

1 A 250m annual alpine grassland AGB dataset over the Qinghai- 2 Tibetan Plateau (2000-2019) in China based on in-situ measurements, 3 UAV ~~images~~photos, and MODIS Data

4 Huifang Zhang^{1,2,3}, Zhonggang Tang², Binyao Wang², Hongcheng Kan², Yi Sun^{1,2}, Yu Qin³, Baoping
5 Meng^{1,2}, Meng Li^{1,2}, Jianjun Chen⁴, Yanyan Lv^{1,2}, Jianguo Zhang^{1,2}, Shuli Niu⁵, Shuhua Yi^{1,2,*}
6

7 ¹Institute of Fragile Eco-environment, Nantong University, 999 Tongjing Road, Nantong, Jiangsu, 226007, China

8 ²School of Geographic Science, Nantong University, 999 Tongjing Road, Nantong, Jiangsu, 226007, China

9 ³State Key Laboratory of Cryospheric Sciences, Northwest Institute of Eco-Environment and Resources, Chinese Academy
10 of Sciences, 320 Donggang West Road, Lanzhou 730000, China

11 ⁴College of Geomatics and Geoinformation, Guilin University of Technology, 12 Jiangan Road, Guilin 541004, China;

12 ⁵Key Laboratory of Ecosystem Network Observation and Modeling, Institute of Geographic Sciences and Natural Resources
13 Research, Chinese Academy of Sciences, Beijing, China
14

15 *Correspondence to:* Shuhua Yi (ysis@ntu.edu.cn)

16 **Abstract.** The alpine grassland ecosystem accounts for 53% of the Qinghai-Tibet Plateau (QTP) area and is an important
17 ecological protection barrier, but it is fragile and vulnerable to climate change. Therefore, continuous monitoring of
18 grassland aboveground biomass (AGB) is necessary. Although many studies have mapped the spatial distribution of AGB
19 for ~~the~~ QTP, the results vary widely due to the limited ground samples and mismatches with satellite pixel scales. This paper
20 proposed a new algorithm using unmanned aerial vehicles (UAVs) as a bridge to ~~re~~-estimate the grassland AGB on the QTP
21 from 2000 to 2019. The innovations were as follows: 1) In terms of ground data acquisition, ~~the~~-spatial scale matching
22 among the traditional ground samples, UAV photos, and MODIS pixels was considered. ~~A During 2015-2019, total of 906-~~
23 ~~pairs~~906 pairs between field harvested AGB and UAV sub-photos, -of quadrat-scale ground-UAV sample data- and 2,602
24 sets of MODIS pixel ~~-scale~~ UAV data (over 37,000 UAV photos) were collected during 2015-2019 ~~(over 37,000 UAV-~~
25 ~~photos)~~. Therefore, the ground validation samples were sufficient and scale-matched. 2) In terms of model construction, the
26 traditional quadrat scale (0.25 m²) was successfully upscaled to the MODIS pixel scale (6,250 m²) based on the random
27 forest and stepwise upscaling methods. Compared with previous studies, the scale matching of independent and dependent
28 variables was achieved, effectively reducing the impact of spatial scale mismatch. The results showed that the correlation
29 between the AGB values estimated by UAV and ~~the~~-MODIS vegetation indices was higher than that between field measured
30 AGB and MODIS vegetation indices at the MODIS pixel scale of the traditional sampling method at the pixel scale. The
31 ~~er~~o~~s~~multis-year validation results showed that the constructed MODIS pixel scale AGB estimation model had good
32 robustness, with an average R² of 0.83 and RMSE of 34.13 g/m²g·m⁻². Our dataset provides an important input parameter for
33 a comprehensive understanding of the role of ~~the~~ -QTP underin global climate change ~~processes~~.

34 from the National Tibetan Plateau/Third Pole Environment Data Center (<https://doi.org/10.11888/Terre.tpdc.272587>, Zhang
35 et al., 2022).

36 **1 Introduction**

37 Grasslands, accounting for approximately 37% of the earth's surface, play an essential role in ~~the~~ global carbon ~~cycle eyeing~~
38 and food supply (Ómara, 2012). However, most natural grasslands have been degraded to a certain extent due to overgrazing,
39 farmland encroachment, soil erosion, and global climate change (Suttie et al., 2005; Ramankutty et al., 2008; Ómara, 2012).
40 Therefore, timely monitoring of grassland health is crucial for ~~the~~ sustainable development ~~of livestock~~ and understanding ~~of~~
41 ~~the~~ global carbon ~~cycleeyeling~~ ~~proeessing~~. Aboveground biomass (AGB) is a key indicator of grassland status and an
42 important input parameter for ecological modeling and carbon storage estimation. Thus, accurate and rapid estimation of
43 AGB is valuable for grassland monitoring.

44
45 The advent of satellites has made it possible to map the spatiotemporal dynamics of grasslands over large areas. Spectral
46 information from different satellites ~~s_sensors~~ -has been employed for biomass estimation, such as Sentinel-2, Landsat, and
47 MODIS (Wang et al., 2019; Zhang et al., 2016). Although there are differences in spatial and spectral resolution, the core
48 idea of ~~_building the a-~~biomass ~~estimation model model~~-is ~~to constructing the~~-linear or nonlinear relationships between the
49 field-measured samples and various satellite spectral indices. Therefore, the ~~estimation~~-accuracy ~~of the estimation~~ is closely
50 related to the quality and quantity of ground samples (Morais et al., 2021; Yu et al., 2021). However, there are still two
51 deficiencies in ground data acquisition: the large spatial gap between the traditional samples and satellite pixels, and the low
52 efficiency.

53
54 How to narrow the spatial gap between traditional samples and satellite pixels is an urgent problem to be solved. Since it is
55 impossible to harvest all grasses within a ~~satellite~~ pixel range, the average of 3-5 quadrats (0.5 m × 0.5 m or ~~1_4~~m × 1_m) is
56 usually used as the measurement (Dusseux et al., 2015; Yang et al., 2017), which results in a considerable spatial gap. A lot
57 of studies have been carried out to upscale ground measurements to satellite pixels (Crow et al., 2012; Bian and Walsh,
58 1993), such as block Kriging geostatistical interpolation, ~~_~~-different types of regression models, ~~or~~-and machine learning
59 algorithms (Cheng et al., 2007; Wang et al., 2014; Cannavacciuolo et al., 1998; Dancy et al., 1986; Li et al., 2018). However,
60 the accuracy of these methods depends on the density of sampling points. In addition, fine-resolution satellites ~~images~~ were
61 used as a bridge to reduce the impact of scale mismatch on AGB estimation (Yu et al., 2021; He et al., 2019). The ~~reason-~~
62 ~~rational~~ is that the finer the ~~satellite~~-resolution ~~of the satellite image~~, the smaller ~~the the~~-spatial gap with the ground samples
63 (Wang and Sun, 2014; Morais et al., 2021). Therefore, ~~obtaining ground samples that match the pixel seale~~~~filling the spatial~~
64 ~~gap between ground samples and satellite pixels~~ -is the key to improving the accuracy of satellited AGB estimation.

65

66 Improving the efficiency of ground sampling is another issue that needs to be addressed. Although the traditional sampling
67 method can yield high-accuracy results, it is time-consuming and labor-intensive. For example, ~~five years were spent in~~
68 ~~completing the collection of ground samples to map the grassland AGB in China~~ Yang et al. spent five years completing
69 ~~the collection of ground samples to invert the grassland AGB in China~~ (Yang et al., 2010). Moreover, with limited original
70 ground data, some scholars had to use the data published by others to ~~increase the sample amount~~ ~~expand the sample size~~
71 (Xia et al., 2018; Jiao et al., 2017). However, datasets from different sources may affect the overall accuracy due to the
72 differences in ~~sample quadrat plot~~ size, ~~plot sample~~ size, and ~~harvesting sampling~~ methods.

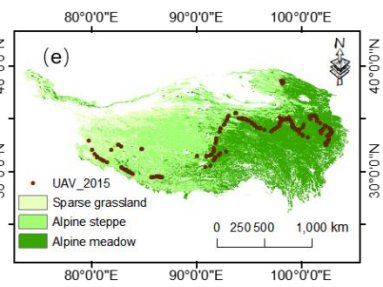
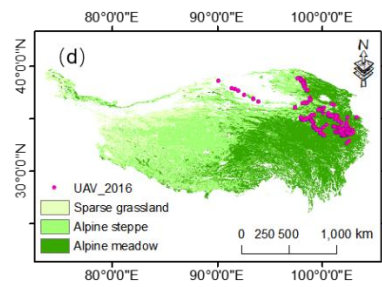
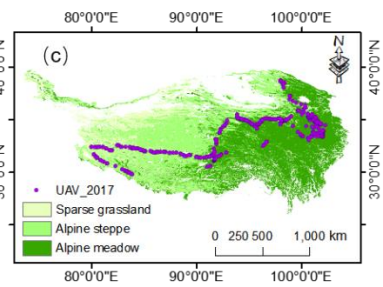
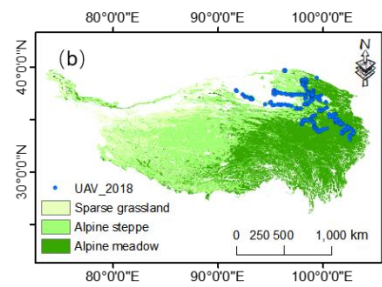
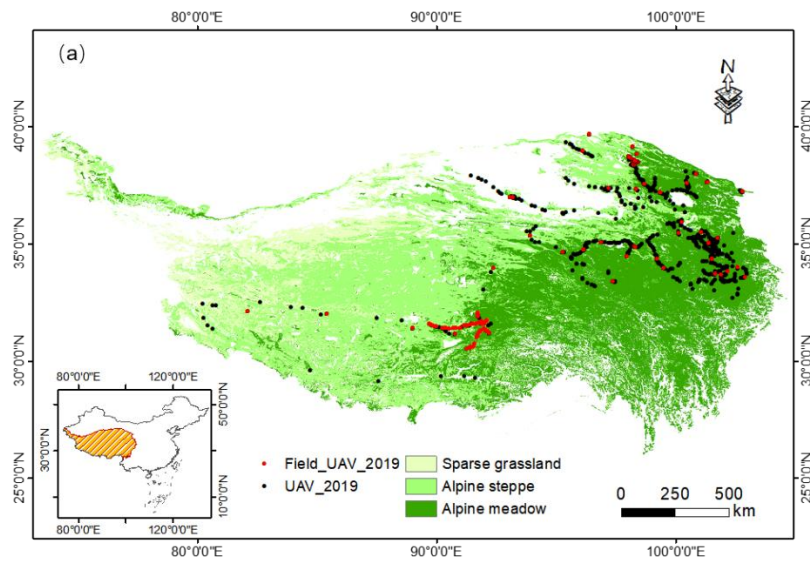
73
74 ~~As a linkage/bridge between field observation and satellites detecting for grassland biomass, the development and popularity~~
75 ~~of unmanned aerial vehicle (UAV) technology has provided a new solution to the abovementioned two issues. The~~
76 ~~development and popularity of unmanned aerial vehicle (UAV) technology has provided new solutions to the above~~
77 ~~problems. UAV photograph images have~~ been successfully used to estimate ecological metrics such as ~~fractional~~
78 ~~vegetation cover (FVC)~~, biomass, and canopy height (Chen et al., 2016; Zhang et al., 2018; Bendig et al., 2015). The use of
79 UAVs has the following ~~two~~ unparalleled advantages over traditional sampling methods. First, UAVs can effectively obtain
80 two- or three-dimensional vegetation information in a non-destructive way, which is helpful for grassland ~~estimation~~
81 ~~monitoring~~ (Lussem et al., 2019; Zhang et al., 2022a; Zhang et al., 2018). Second, UAVs can rapidly collect key parameters
82 of grassland within satellite pixels (e.g., FVC, Chen et al. 2016). Hence, UAV ~~photographs images~~ can serve as a bridge to
83 ~~reduce-fill~~ the spatial gap between field samples and satellite pixels. However, most current UAV-based grassland biomass
84 estimations are ~~conducted on a small scale, but few studies are on a regional scale~~ ~~small-scale, with few regional-scale~~
85 ~~studies~~. Whether UAVs can be used to ~~reducefill~~ the spatial gap between traditional ground sampling and satellite pixels
86 remains an open question. In addition, ~~previous studies~~ ~~there is a shortage of~~ ~~multi-year validation~~ ~~lacked~~ ~~cross-year~~
87 ~~validation~~ to test the robustness of the AGB estimation model over time ~~due to the limited sample amount in previous~~
88 ~~studies~~ ~~due to the limited sample size~~.

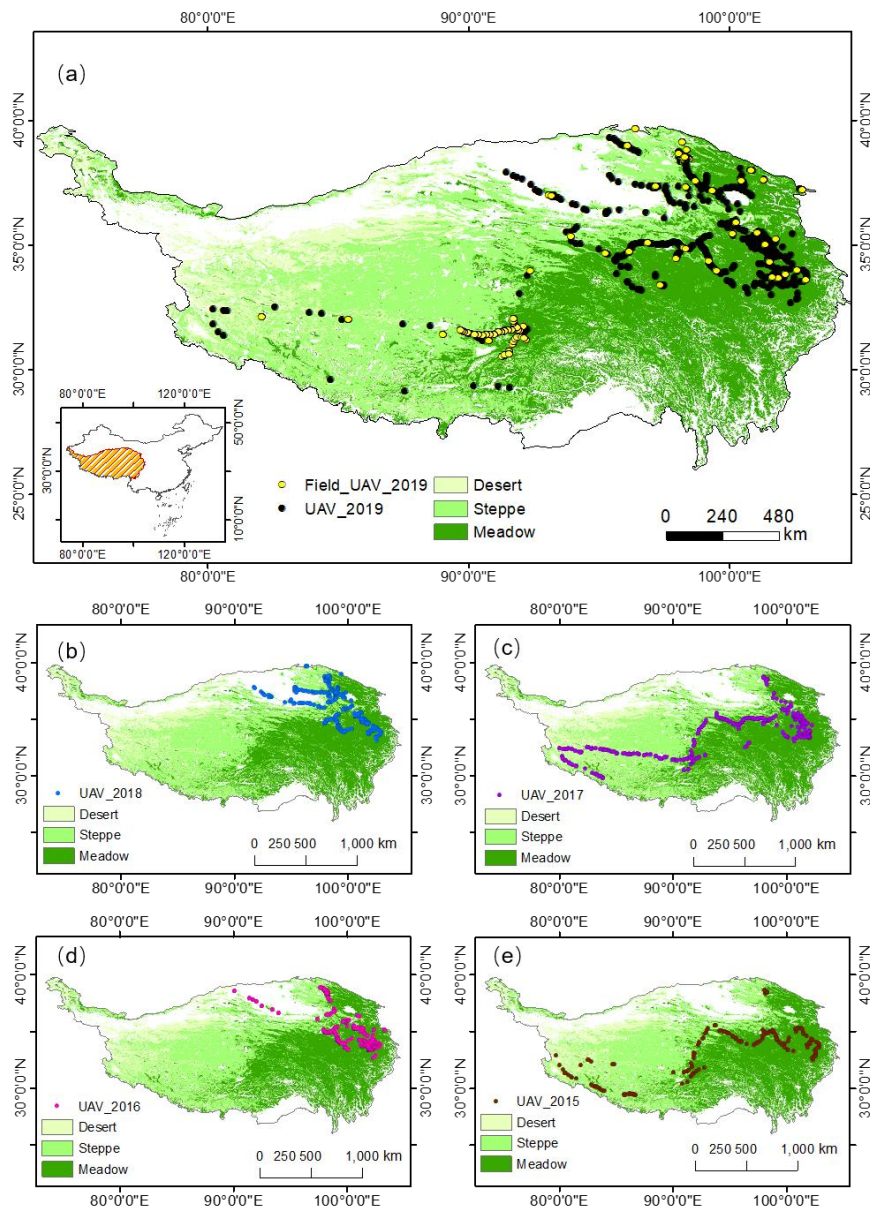
89
90 This study proposed a new approach ~~that combines~~ ~~combining~~ traditional ground sampling, UAV photography, and satellite
91 ~~image data~~ to produce a new reliable AGB dataset ~~for the grasslands of the Qinghai-Tibetan Plateau (QTP)~~ ~~of QTP grassland~~.
92 The objectives of this study were: 1) to construct a UAV-based grassland AGB estimation model at the quadrat/~~satellite~~
93 ~~MODIS~~ pixel scales, respectively; 2) to investigate whether UAVs can be used as a bridge to ~~reduce-fill~~ the spatial gap
94 between ground samples and satellite pixels to improve the accuracy of grassland AGB ~~estimation~~, and 3) to map the AGB
95 of alpine grasslands on the ~~Qinghai-Tibetan Plateau (QTP)~~ from 2000 to 2019.

96 2 Materials and Methods

97 2.1 Study Site

98 QTP is the highest and largest plateau on the earth (26°00'12"~39°46'50"N, 73°18'52"~104°46'59"E), with an average
99 elevation of ~4000 m and an area of approximately 257.24×10^4 km² (Figure 1). It is located in western China, with an
100 average annual temperature and precipitation of about 1.6°C and 413.6 mm, respectively. The ~~primary main~~-grassland types
101 are ~~alpine meadows~~, ~~alpine steppe~~, and ~~sparse desert grassland~~, which play a critical role in climate regulation, water
102 conservation, and biodiversity protection (Ding et al., 2013). In this study, the boundary of the QTP ~~of China~~ (Zhang et al.,
103 2014) was downloaded from the National Earth System Science Data Center, National Science & Technology Infrastructure
104 of China (<http://www.geodata.cn>). Grassland types ~~s_data-wascre~~ derived from the 1:1000000 Chinese digital grassland
105 classification map provided by the China Resource and Environmental Science and Data Center (<https://www.resdc.cn/>).
106 This data-set, generated through field surveys in the 1980s and supplemented by satellite and aerial imagery, is the most
107 detailed grassland--type map available. ~~To facilitate comparison with others' AGB estimates~~~~For comparison with others~~, we
108 ~~regrouped ecombined~~ the grassland types into three categories: ~~alpine meadow~~, ~~alpine steppegrassland~~, and ~~sparse desert~~
109 ~~(Table A1)grassland~~, and ~~resampled to 250 m~~~~resampled this regrouped vector to a grid with 250 m spatial resolution~~(~~Table~~
110 ~~A1~~).





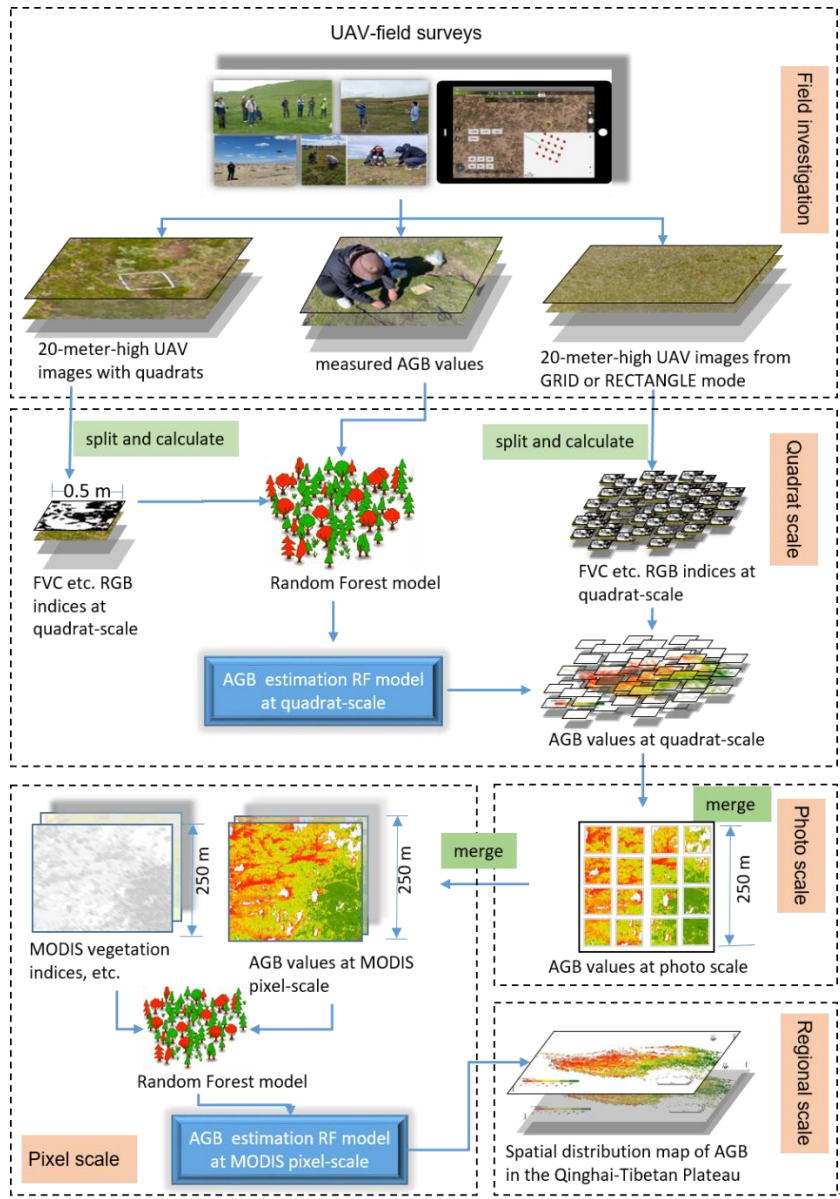
112

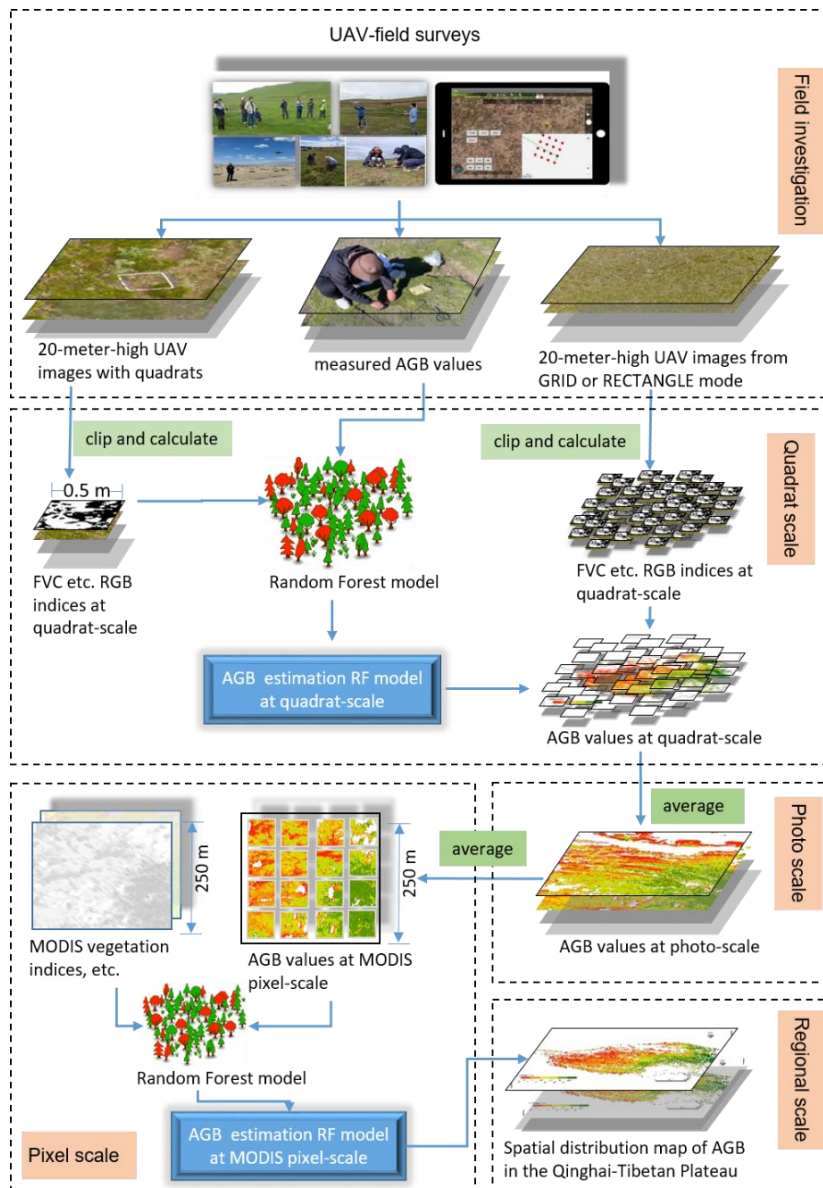
113 **Figure 1. Distribution of field and UAV sampling sites in 2019 (a); UAV sampling sites in **alpine** grasslands on the QTP from 2015-**
 114 **2018 (b-e). Field_UAV_2019 represents the quadrat-scale sampling sites for the 2019 UAV-Field synchronous grassland biomass**
 115 **experiment. UAV_year represents the UAV sampling points based on the GRID or RECTANGLE mode of the corresponding year.**

116 2.2 Overall technology roadmap

117 **Figure 2 was t**he overall flowchart of this study **is shown in Figure 2.** It consisted of four main steps: 1) UAV and field
 118 investigation; 2) constructing the AGB estimation model at the quadrat scale; 3) upscaling the grassland AGB to the MODIS

119 | pixel scale [\(250 m\)](#); 4) building the AGB estimation model at the MODIS pixel scale [\(250 m\)](#) and applying it to the QTP
120 | region. More detailed information [on about](#) each step was described in the following sections.





122
123
124
125

Figure 2. The overall flowchart of UAV field survey and the construction of grassland AGB estimation models at different spatial scales.

126 **2.3 Field investigation**

127 **2.3.1 UAV and route planning**

128 DJI Phantom 3 Professional (DJI Company, Shenzhen, China), a popular consumer quadrotor UAV with a high-resolution
129 RGB camera, was used to collect UAV photos images of the QTP from 2015 to 2019. It has a 1/23-inch CMOS sensor and is
130 capable of taking 12-megapixel photos. In addition, it uses a 3-axis stable gimbal to take photos vertically downward to

131 eliminate the distortion of UAV ~~photos~~images. It has good environmental adaptability, with an operating temperature range
 132 from 0°C to 40°C, and a maximum take-off altitude of 6000 meters. Therefore, DJI Phantom 3 Professional is
 133 ~~adequately~~ adapted to ~~monitor grassland states the low temperature and high altitude of~~on the QTP. More detailed
 134 information about the UAV system was listed in Table A2.

135
 136 Fragmentation ~~m~~Monitoring and ~~a~~Analysis with aerial ~~p~~Photography (FragMap) system, ~~capable of long-term collaborative~~
 137 ~~observation~~, was used for UAV route planning (Yi, 2017). During 2015-2019, we conducted UAV monitoring of the QTP
 138 grasslands using FragMap (Figure 1). Over 2,000 fixed flight routes were set up during this period, and more than
 139 ~~37,000~~40,000 UAV ~~photos~~ images were collected, providing a ~~sufficient~~ reliable UAV dataset for this study (Table 1).

140

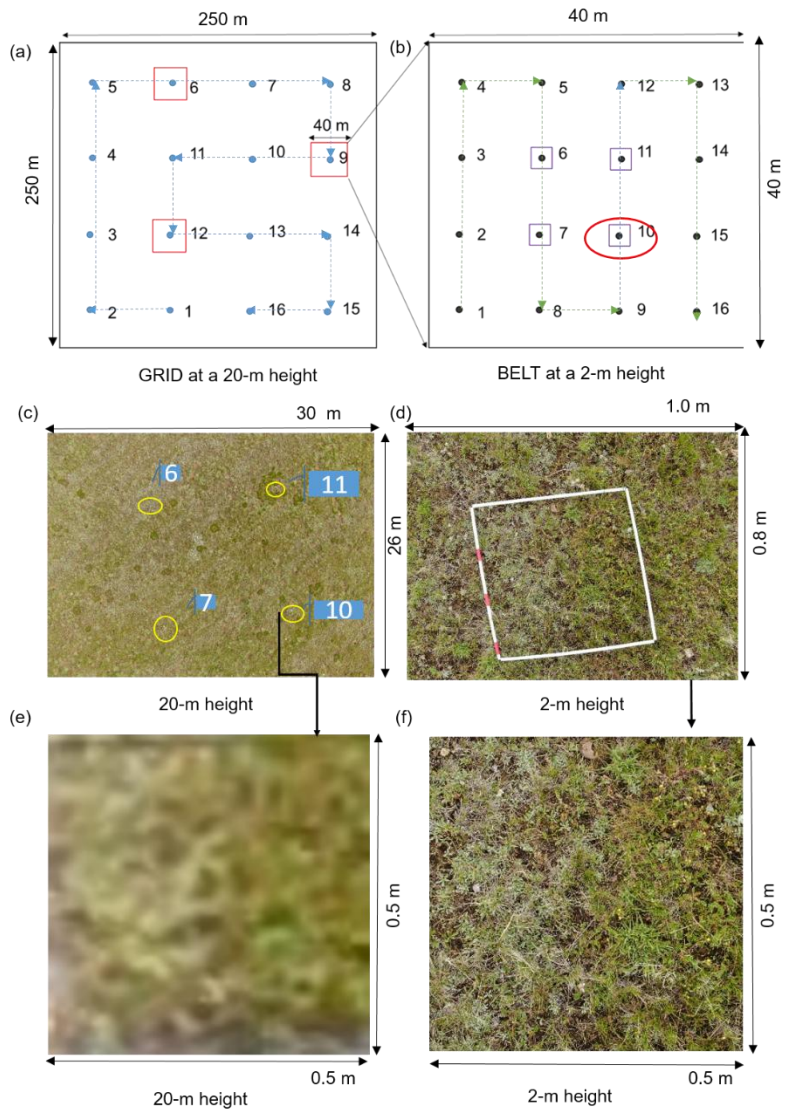
141 **Table 1. UAV sampling information from 2015 to 2019**

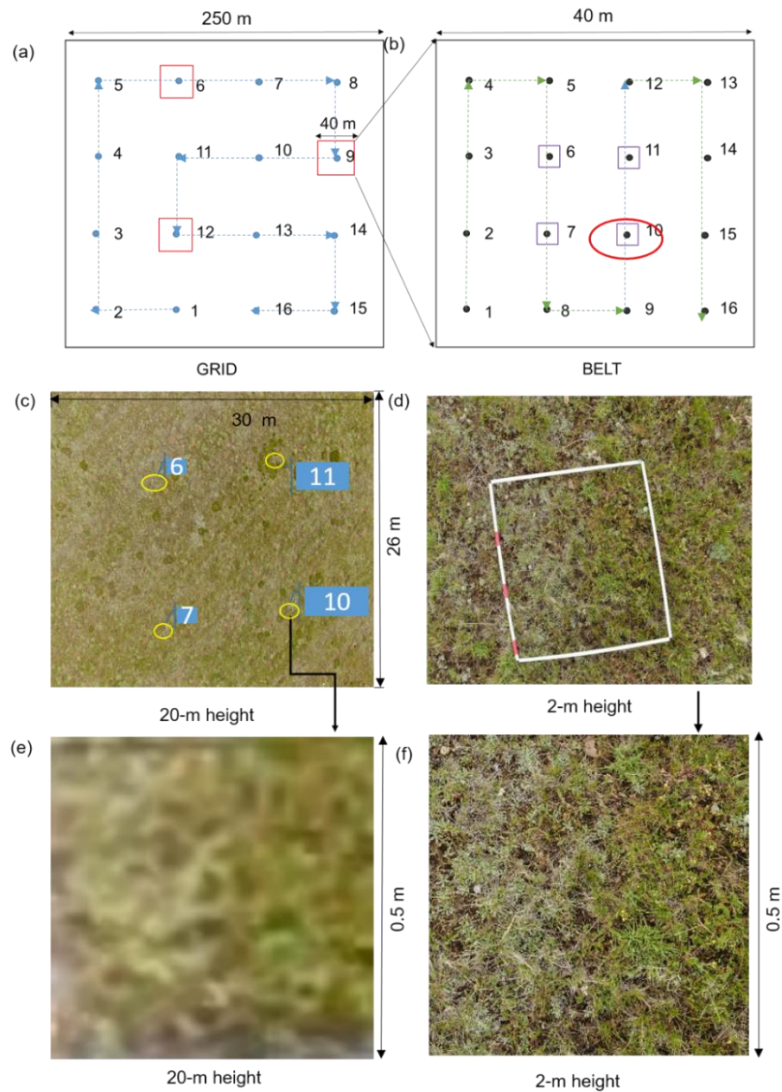
Year	Flight Mode	Number of routes	Photo number	Acquisition time date
2015	RECTANGLE	214	2568	7/05 ~ 8/24
2016	RECTANGLE	334	4008	6/20 ~ 9/29
	GRID	150	2400	6/20 ~ 9/23
2017	RECTANGLE	315	3780	5/10 ~ 10/24
	GRID	322	5152	7/15 ~ 8/22
2018	RECTANGLE	79	948	7/22 ~ 8/03
	GRID	303	4848	7/04 ~ 8/29
2019	GRID	885	14160	7/12 ~ 9/21
	BELT	151	2416	7/12 ~ 9/21
Total	Total	26022753	3786440280	

142

143 GRID, RECTANGLE, and BELT are the most ~~commonly~~ widely used flight modes in ~~the~~ FragMap software. ~~Among these~~
 144 ~~modes~~, GRID and RECTANGLE modes have 16 and 12 waypoints for capturing UAV ~~photos~~images within a MODIS pixel
 145 range (250 m × 250 m) (Figure A1). ~~Their~~ The flying height and speed are set to 20 m and 3 m/s, respectively. The spatial
 146 coverage ~~area~~ of a 20-meter-high UAV photo is about 26 m × 35 m. The BELT mode is similar to GRID, but is designed to
 147 obtain near-ground UAV ~~photos~~ image ~~data~~ with higher resolution (Figure 3b). ~~It can be combined with the traditional~~
 148 ~~sampling method to ensure the consistency of UAV images with the ground samples (Figure 3d). Normally~~Typically, the
 149 BELT size is set to 40 m × 40 m, and the flying height and speed are set to 2 m and 1 m/s ~~to~~ to ensure that field crews have
 150 enough time to place sampling ~~quadrats~~ frames under the UAV waypoints. ~~Therefore, it can be used to help field workers~~
 151 ~~quickly and evenly place sampling quadrats~~. As with the GRID mode, 16 UAV ~~photos~~ images can be captured in a single

152 | flight of BELT. Compared with the MOSAIC ~~flight~~ mode (which requires a guaranteed overlap rate between photos to
153 | obtain a full view of an area), our design is more in line with the traditional ecological sampling concept and more conducive
154 | to rapid sample collection. ~~It allows for a better balance of spatial representation and accessibility of samples, resulting in~~
155 | ~~efficient sample collection~~.





157
 158 **Figure 3. Schematic diagram of the UAV-field synchronization experiment in 2019: a combination design of GRID (a) and BELT**
 159 **(b) flight modes; a UAV image-photo with a quadrat from the BELT mode at the height of 2 m (d); a 20-meter-high UAV image-**
 160 **photo including four sample quadrats (c); and the cropped UAV images-photos at the quadrat scale from 20 m (e) and 2 m (f)**
 161 **height, respectively.**

162 2.3.2 Synchronization experiment of UAV and field sampling

163 A UAV-field biomass synchronization experiment was designed-conducted in 2019 to ensure spatial matching among
 164 satellites, UAVs, and ground sampling (Figure 3). The specific implementation-four steps were as follows. First~~ly~~, we set a
 165 GRID flight mode with a MODIS pixel size (250 m × 250 m) (Figure 3a). ThenSecondly, three waypoints were randomly-
 166 selected from the GRID -flight mode - to set the BELT flight modes (40 m × 40 m). For each BELT, a sampling frame-
 167 quadrat (0.5 m × 0.5 m) was placed at its 6, 7, 10, and 11 waypoints to ensure that the GRID image-photo could contain the

168 four ~~above~~mentioned ~~quadrats above~~ (Figure 3b-c). ~~Then~~ ~~Thirdly~~, ~~after the implementation of all flights at the end of~~
169 ~~all flights~~, the grassland AGB samples were cut, bagged, and numbered. Finally, these samples were oven-dried at 65°C to
170 constant weight to obtain the field-measured AGB values.

171

172 2.4 Data processing

173 2.4.1 UAV photo pre-processing and indices calculation

174 Pre-processing of UAV photos included image quality inspection, cropping, and calculation of different indices. ~~It should be~~
175 ~~noted that only UAV photos at 20 m height were used in this paper.~~ Firstly, we eliminated overexposed or blurred 20-meter-
176 high UAV ~~images~~photos. Secondly, the pixels in the sampling ~~quadrats frames~~ were cropped and saved (Figure 3e). Thirdly,
177 the RGB indices, ~~including color space, histogram, and vegetation indices, for the cropped UAV images~~photos were
178 calculated. ~~Similar to based on the method in~~ our previous study (Zhang et al., 2022a), ~~indices included color space,~~
179 ~~histogram, and vegetation indices, the details of which can be found in Zhang et al. (2022a).~~ In addition, 30 other RGB
180 ~~vegetation~~ indices were added as candidate independent variables. The names, formulas, and references of the above indices
181 ~~were~~ ~~are~~ shown in Table A3.

182 2.4.2 MODIS vegetation index and other spatial data

183 The MOD13Q1(v006) product was downloaded from ~~the~~ ~~NASA~~ ~~the National Aeronautics and Space Administration (NASA)~~
184 earth explorer website (<https://earthexplorer.usgs.gov/>) ~~for~~ ~~detecting inversion of~~ the alpine grassland AGB on the QTP. The
185 data contained two commonly used vegetation indices, the Normalized Vegetation Index (NDVI) and the Enhanced
186 Vegetation Index (EVI), with spatial and temporal resolutions of 250 m and 16 days, respectively. A total of 2,842 scenes
187 from 2000 to 2019 were downloaded. Then, the MODIS images were reprojected and ~~mosaicd~~ ~~stitched~~ using the MODIS
188 Projection Tool (MRT). After that, the corresponding vegetation indices closest to the ~~time-date~~ of the UAV sampling were
189 extracted to construct/validate ~~a~~ ~~the~~ MODIS pixel-scale AGB estimation model. ~~In~~ addition, the kNDVI ~~index~~ was
190 calculated to overcome the NDVI saturation issue based on the equation $kNDVI = \text{TANH}(NDVI^2)$ (Camps-Valls et al.,
191 2021). The annual maximum vegetation indices were calculated by the maximum value composition (MVC) algorithm to
192 estimate the spatial AGB distribution of ~~the~~ QTP from 2000 to 2019 (Holben, 1986; Wang et al., 2021; Gao et al., 2020).

193

194

195 Furthermore, ~~the~~ meteorological, ~~the~~ soil texture, ~~the~~ and topographic data were ~~also~~ included as candidate independent variables for
196 constructing ~~the~~ ~~the~~ MODIS pixel-scale AGB estimation model. Meteorological factors, including ~~annual~~ mean ~~annual~~
197 temperature (MATTA), ~~annual~~ mean ~~annual~~ precipitation (MAPPREC), and ~~annual~~ total ~~annual~~ solar radiation (TASRRAD),
198 were calculated based on the daily meteorological dataset from the National Meteorological Information Center of China

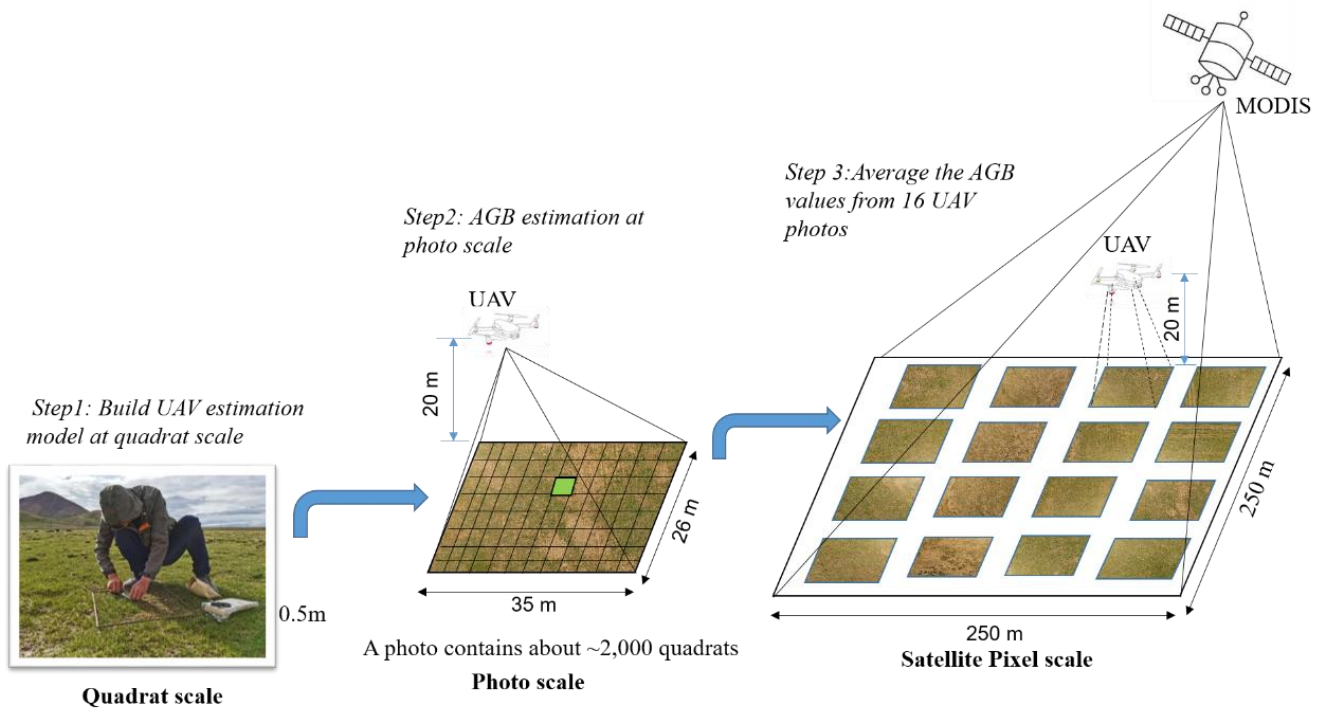
199 | (<http://data.cma.cn/>). The data processing steps mainly included ~~checking and eliminating the anomalous values of attributes,~~
200 | ~~interpolation,~~ cumulative summation, ~~and~~ annual ~~_~~averaging, ~~and interpolation~~ to obtain a meteorological raster dataset with
201 | a spatial resolution of ~~1000-1 meters km~~ (Li et al., 2021). Moreover, soil texture data at 1 km spatial resolution, including the
202 | ratio of soil organic matter (SOM), clay, sand, and silt, were downloaded from the Resource and Science and Data Center of
203 | China (<https://www.resdc.cn/>). All the meteorological and soil ~~raster~~ datasets were ~~regridded _resampled_~~ into 250 m by
204 | ArcGIS software ([Version 10.2, Environmental Systems Research Institute, Inc.](#)) to match the MODIS ~~imagedata~~.

206 | ~~Terrain factors _including altitude, slope, and aspect, were derived from the digital elevation model (DEM) using the terrain~~
207 | ~~analysis tool of ArcGIS software. Terrain factors included the digital elevation model (DEM), slope, and aspect.~~ The DEM
208 | was ~~retrieved derived~~ from Shuttle Radar Topography Mission (SRTM) imagery (version 004, 90 m) and ~~regridded~~
209 | ~~resampled~~ to 250 m. ~~The slope and aspect data were derived from DEM data using the terrain analysis tool of ArcGIS~~
210 | ~~software.~~

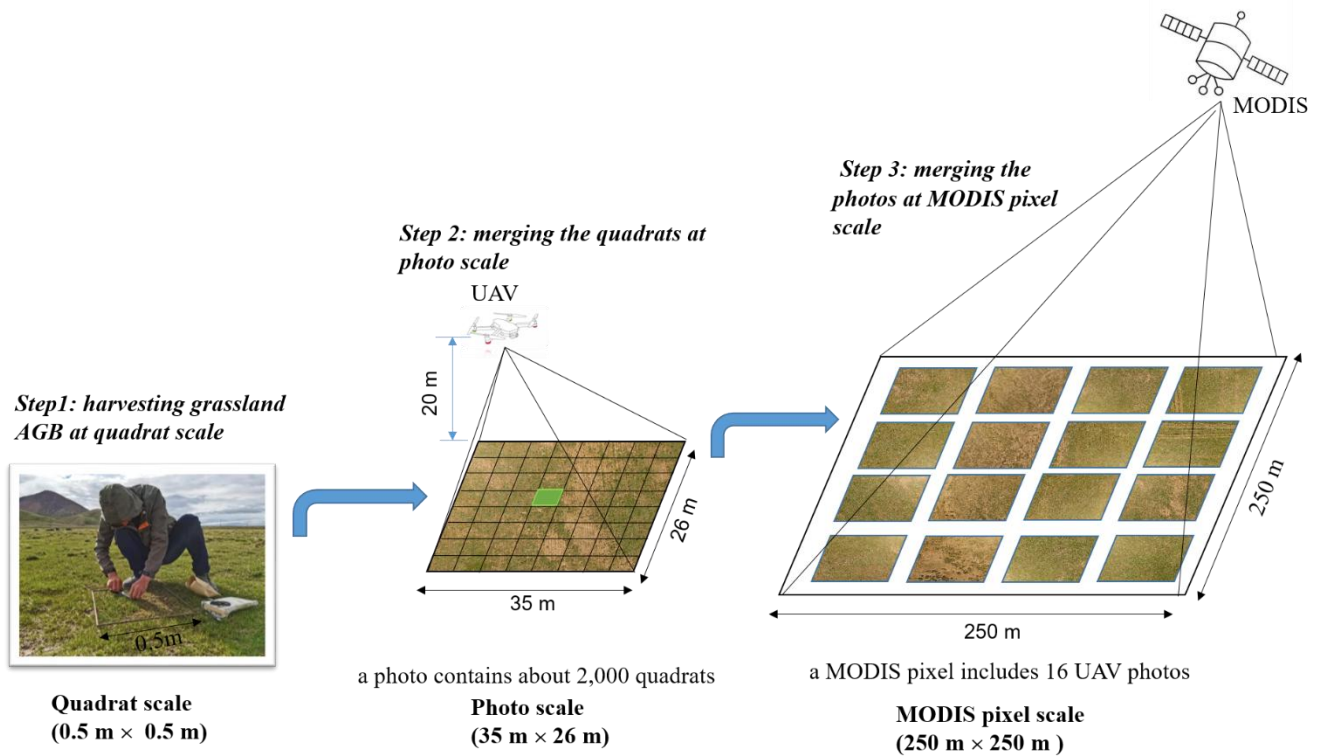
211 | **2.5 AGB modeling and computation at different scales**

212 | We estimated the grassland AGB at three scales: the quadrat scale, the photo scale, and the ~~satellite~~-MODIS pixel scale
213 | (Figure 4). More detailed information was described as follows.

214



215



216

Figure 4. Upscaling steps to estimate grassland AGB matching the MODIS pixel scale.

217 **2.5.1 Modeling method-Random forest model**

218 Random Forest (RF) (Breiman, 2001) is an ensemble-learning algorithm that has been widely used to estimate AGB due to
219 its excellent performance (Ghosh and Behera, 2018; Mutanga et al., 2012; Wang et al., 2016). The two ~~main-primary~~
220 parameters, ~~namely-named~~ the number of regression trees in the forest (*ntree*) and the number of feature variables required
221 to create branches (*mtry*), were first~~ly~~ optimized based on the root mean square error (RMSE) of training data. Here, the
222 value of ~~ntree~~ was set from 100 to 5000 with an interval of 100, while *mtry* was set as the square root of the number of
223 training sample features. In addition, the importance of each predictor was ranked by calculating the percentage ~~increased~~
224 ~~increase~~ in mean square error (%IncMSE).

225
226 The backward feature elimination method (BFE) was used to reduce the number of input variables to simplify the RF model
227 (Vergara and Estévez, 2014). The ~~main-primary~~ steps were as follows: 1) constructing an AGB RF model by including all
228 predictors ~~variables~~ in the initial stages and calculating the %IncMSE ~~index~~ for each variable; 2) eliminating the least
229 promising variable and then rerunning the RF model until only one independent variable was left. Moreover, the
230 corresponding coefficient of determination (R^2) and the corresponding RMSE ~~—~~ were calculated in each iteration; ~~;~~ 3) the
231 smallest subset of variables with the highest R^2 was selected as the final optimized indices.

232
233 In addition, different training and validation strategies were used at different scales. ~~At the quadrat scale, a 10-fold cross-~~
234 ~~validation method was used~~ 10-fold cross-validation method was used at the quadrat scale due to the limited ground samples
235 (Kohavi, 1995). At the MODIS pixel scale, 30% of the UAV-estimated AGB samples in 2019 were randomly selected as an
236 independent validation dataset due to ~~its large size~~ the large sample size. Meanwhile, the UAV_AGB values from 2015 to
237 2018 were used for ~~eross~~ multi-year validation to test the robustness of the model over time. Statistical metrics R^2 (Eq.1) and
238 RMSE (Eq.2) were used to evaluate ~~the performance of the model~~ model's performance.

$$239 \quad R^2 = 1 - \frac{\sum_{i=1}^n (\hat{y}_i - y_i)^2}{\sum_{i=1}^n (\hat{y}_i - \bar{y})^2} \quad (1)$$

$$240 \quad RMSE = \sqrt{\frac{\sum_{i=1}^n (\hat{y}_i - y_i)^2}{n}} \quad (2)$$

241 ~~where~~ where n is the number of samples, y_i and \hat{y}_i represent the measured and the predicted AGB value, respectively, \bar{y} is
242 the ~~mean value~~ mean value of measured AGB samples.

243 **2.5.2 AGB RF estimation model at the quadrat scale (0.25 m²)**

244 Since the spatial coverage area of a 20-meter-high UAV photo (26 m \times 35 m) is much ~~wider-larger~~ wider-larger than a single 2-meter-
245 high UAV photo (0.8 m \times 1 m), making it easier to match ~~to~~ the MODIS pixel scale (250 m \times 250 m). Hence, the 20-meter-
246 high UAV photos containing the sample ~~quadrats frames~~ were chosen for constructing the quadrat-scale AGB estimation
247 model. A total of 906 pairs between field harvested AGB and UAV sub-photos of quadrat-scale UAV field AGB observation

248 ~~data~~ were collected, with good spatial representativeness (Figure 1-a, ~~yellow~~red dots). The observed AGB values ranged
249 from 0 to 450 $\text{g}\cdot\text{m}^{-2}\text{g}/\text{m}^2$, with mean and median values of 59.75 $\text{g}\cdot\text{m}^{-2}\text{g}/\text{m}^2$ and 33.04 $\text{g}\cdot\text{m}^{-2}\text{g}/\text{m}^2$, respectively, ~~most of which~~
250 ~~were less than 100 g/m^2~~ (Figure 5a). The cropped 20-meter-high UAV ~~image-photo~~ indices and the measured AGB values
251 were used as the independent and dependent variables to build the RF model at the quadrat scale (Figure 2).

252 2.5.3 AGB calculation at the photo scale (~900 m²)

253 The steps for AGB estimation of the whole 20-meter-high UAV photo were as follows: 1) First~~ly~~, each UAV photo was
254 ~~divided-split~~ into ~2,000 quadrat-sized small patches. 2) Second~~ly~~, the AGB of each small patch was calculated based on the
255 quadrat-scale AGB estimation model. 3) Finally, the average of all small patches was calculated as the AGB of the whole
256 photo. Based on the above steps, the AGB values of more than 75 million quadrats in 37,864 photos in GRID or Rectangle
257 mode were calculated using more than 75 million AGB values of the UAV quadrat scale (Table 1)~~Based on the above steps,~~
258 ~~the AGB values of 37,487 images in GRID or Rectangle mode were calculated using more than 74 million AGB values of~~
259 ~~the quadrat scale (Table 1).~~

260

261

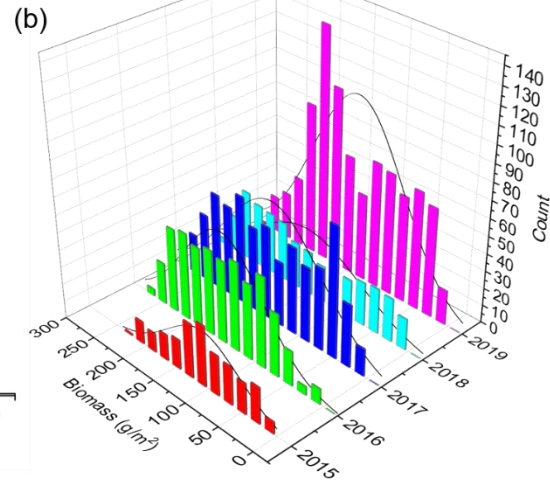
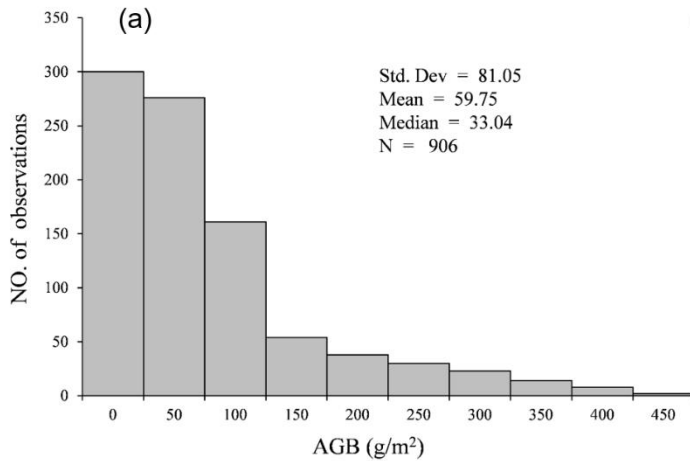
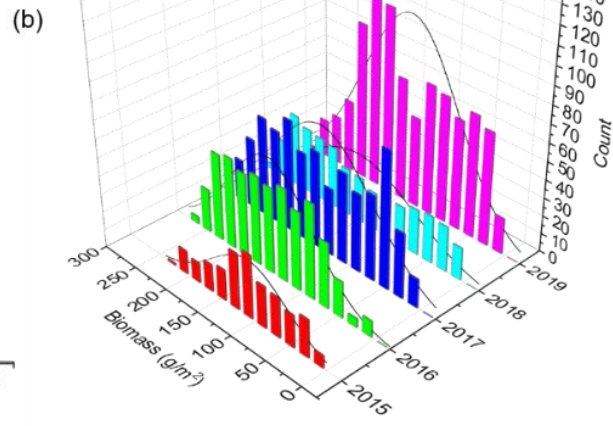
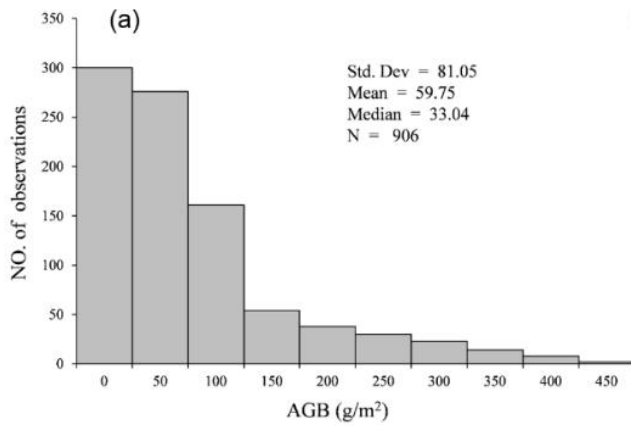


Figure 5. Histograms of field-measured AGB values at quadrat scale (a) and UAV-estimated AGB values of different years at the photo scale (b).

2.5.4 AGB RF model construction at MODIS pixel-scale (6,2500 m²)

The following steps were involved in constructing the AGB estimation model at the MODIS pixel scale. 1) Since the coverage area of a GRID or RECTANGLE mode was similar to that of a MODIS pixel, the average value of 16 or 12 UVA photos' AGB was taken as the AGB value of the corresponding MODIS pixel. During 2015-2019, a total of 2,602 UAV-estimated AGB samples

272 were obtained at the MODIS pixel scale (Table 1). 2) The MODIS vegetation indices and other spatial metrics (such as
273 meteorological, ~~soil texture,~~ and topographic data) corresponding to each GRID or RECTANGLE mode were then
274 extracted using the ArcGIS software. Here, the MODIS NDVI, EVI, and kNDVI indices closest to the sampling ~~time-date~~
275 were chosen to minimize the time difference between sampling and satellite overpass. 3) Subsequently, the UAV-estimated
276 AGB values, ~~the MODIS vegetation indices-extracted-spatial-indices,~~ and other spatial metrics were used as dependent and
277 independent variables to build ~~the the~~-AGB estimated model at ~~the the~~-MODIS pixel scale using the RF ~~algorithm~~ model.

278 2.6 Uncertainty analysis

279 Since the actual AGB values of MODIS pixels cannot be directly obtained, ~~the regression coefficient between vegetation~~
280 ~~indices and estimated AGB vegetation indices-were~~ was used to quantify the uncertainty of different AGB estimation
281 methods. In other words, the higher the correlation between the estimated AGB and MODIS vegetation indices, the more
282 accurate the estimation model was. The performance of the estimation model was evaluated through three aspects. In this
283 study, we first compared the correlation between the MODIS vegetation indices and AGB values obtained by traditional
284 sampling and UAV estimation methods. We also explored the uncertainties of UAV sampling coverage ~~area~~ -by ~~regularly~~
285 ~~randomly~~ combining the number of photos in a MODIS pixel, and tested whether the estimated AGB was closer to the “true”
286 value as the number increased. Furthermore, the AGB validation results ~~from-between~~ GRID ~~or-and~~ RECTANGLE at the
287 pixel scale were compared to understand the uncertainties caused by different flight modes.

288 2.7 Trend analysis of grassland AGB

289 This study combined the Theil-Sen median trend analysis and Mann-Kendall test to analyze the temporal variation
290 characteristics of grassland AGB ~~of-in~~ QTP (Jiang et al., 2015). Theil-Sen median trend analysis is a robust trend statistical
291 method with high computational efficiency, insensitive to outliers (Hoaglin et al., 1983). The Mann-Kendall test is a
292 nonparametric test for time series trends, which does not require the measurements to follow a normal distribution and is not
293 affected by missing values and outliers. The Theil-Sen Median trend analysis and Mann-Kendall trend test have been widely
294 used to analyze ~~the temporal trend of~~ vegetation index, cover, and biomass (Gao et al., 2020; Jiang et al., 2015; Fensholt et
295 al., 2009). The ~~detailed~~ formulas for the Theil-Sen median trend analysis and the Mann-Kendall method are ~~detailed~~
296 ~~provided by in~~ Jiang et al. (2015).

297 3 Results

298 3.1 Independent variables selected for AGB modeling

299 The independent variables for AGB estimation at the quadrat and MODIS pixel scales were presented in Table 2. A total of
300 36 independent variables were selected at the quadrat scale, including 26 vegetation RGB indices, ~~6-six~~ histogram indices,

301 | and ~~4-four~~ color space indices (Figure A2). At the MODIS pixel scale, ~~5~~-five variables were selected, including NDVI,
302 | kNDVI, EVI, PRECMAP, and DEM (Figure A3).
303 |
304 |

305 Table 2: Selected independent variables for the AGB modeling at quadrat and pixel scales. The full names of each variable at the
 306 quadrat scale were listed in Table A3.

Scale	Model	Number	Independent variables
Quadrat	RF _Q	36	FVC, WI, GI, EXG, TGI, EXGR, VEG, GRATIO, COM, CIVE, RGBVI, EXR, GLA, GRRI, MVARI, MGRVI, GRVI, RGRI, GBRI, VARI, NDI, RRATIO, EXB, V, IPCA, INT, HOC_R_CORR, HOC_B_CHIS, HOC_R_CHIS, HOC_G_CHIS, HOC_G_CORR, HOC_B_CORR, B, H, G, R;
Pixel	RF _{PP}	5	NDVI, kNDVI, EVI, DEM, MAPPREC

307

308 3.2 Modeling and accuracy assessment

309 For the AGB estimation model at the quadrat scale, the results of 10-cross validations showed that there was a significant
 310 linear relationship between the estimated and the field measured values ($R^2 = 0.73$, $p < 0.001$, Table 3, Table A4). ~~The~~
 311 ~~student's t-test was also used to assess whether there was a significant difference between the predicted AGB values and the~~
 312 ~~measured values at a confidence level of 95%. As shown in Table 4, there was no significant difference ($p = 0.51 > 0.05$)~~
 313 ~~between the predicted AGB values and the measured values of the mean AGB at a confidence level of 95% (Table 4)~~
 314 with an RMSE of $-32.94 \text{ g}\cdot\text{m}^{-2}$ (Table 3). ~~The scatter plot showed that the~~ model predicted well when the measured
 315 biomass was less than $150 \text{ g}\cdot\text{m}^{-2}$, ~~but however, showed some~~ underestimation was found when the measured biomass
 316 was more than $200 \text{ g}\cdot\text{m}^{-2}$ (Figure 6a). It may be because the number of samples more than $200 \text{ g}/\text{m}^2$ is relatively small,
 317 accounting for only 8.50% of all samples (Figure 5a). Although the sample amount size of UAVs varied ~~from~~ year to by year,
 318 ~~most of~~ the AGB values estimated from UAV photos typically ranged from 0 to $300 \text{ g}\cdot\text{m}^{-2}$ (Figure 5b).

319

320 For the AGB estimation model at the MODIS pixel-scale ~~AGB estimation model~~, there was a strong linear relationship ($p <$
 321 0.05) between the estimated AGB predicted ~~AGB~~ and that measured by UAV photos ~~estimates~~ for 2015-2019 (Table A4).
 322 The fitting coefficient R^2 was 0.85 for 2017-2019, ~~and~~ slightly lower for 2015-2016 at with the value of 0.63 and 0.77,
 323 respectively (Table 3, Figure 6b-f). ~~The RMSE of the pixel-scale model ranged from~~ 23.36 ~~to~~ $34.07 \text{ g}\cdot\text{m}^{-2}$ (Table 3). In
 324 addition, we found no significant differences ($p > 0.05$) between the predicted and measured values of the average ~~average~~
 325 AGB, values ~~except for 2017 and 2018~~ (Table 4). The average values of AGB estimated by the MODIS pixel-scale model
 326 for 2017 and 2018 were $131.48 \text{ g}\cdot\text{m}^{-2}$ and $120.60 \text{ g}\cdot\text{m}^{-2}$, which were 14.72% and 13.78% lower than those ~~of~~ estimated by
 327 UAV photos, respectively. Although the estimated average AGB estimates there were differences between the MODIS
 328 pixel-scale model estimates and UAV were different estimates in 2017 and 2018, the error percentages were
 329 acceptable. While the average model projections for 2017 and 2018 were 14.72% and 13.78% lower than the UAV estimates,

330 ~~they were within acceptable ranges.~~ Therefore, the constructed MODIS pixel-scale AGB estimation model had good
331 performance and robustness in different years (Figure 6b--f).

332

333

334

335

336

337 **Table 3. Validation results of AGB models at the quadrat and pixel scales**

Scale	Year	Training set		Validation set	
		R ²	RMSE(<u>g·m⁻²g/m²</u>)	R ²	RMSE(<u>g·m⁻²g/m²</u>)
Quadrat-scale	2019	0.94	20.18	0.73 ***	32.94
Pixel-scale	2019	0.96	10.68	0.85 ***	23.36
	2018	—	—	0.85 ***	24.83
	2017	—	—	0.85 ***	23.83
	2016	—	—	0.77 ***	31.28
	2015	—	—	0.63 ***	34.07

338 '***' significant at p < 0.001

339

340

341 **Table 4. T-test results between the predicted and measured AGB values for the modes at the quadrat and pixel scales**

Validation model	Measured mean (<u>g·m⁻²</u>)	Predicted mean (<u>g·m⁻²</u>)	t	df	p-value
2019_Quadrat-scale	51.57	54.35	-0.66	939.35	0.51
2019_Pixel_scale	136.68	137.746175	-0.15	340.78	0.88
2018_Pixel_scale	152.49	131.48	4.01	723.81	6.63e-05
2017_Pixel_scale	141.42	120.60	5.48	1225.20	5.26e-08
2016_Pixel_scale	149.56	142.70	1.68	961.99	0.09413
2015_Pixel_scale	108.65	98.23	1.96	1225.20	0.05

342

343

344 **3.3 Correlation analysis between AGB values and MODIS indices**

345 The correlations between the UAV-estimated AGB values and MODIS vegetation indices were much better than that
346 between field harvested AGB and MODIS vegetation indices the traditional sampling method (Figure 7a). For example, the
347 correlation between NDVI and field harvested traditionally measured AGB was only 0.53, considerably lower than the
348 correlation between NDVI and AGB obtained from a single UAV photo much lower than that obtained from a single UAV
349 image (r = 0.74). Moreover, the correlation between NDVI and UAV-estimated AGB increased with the increasing with the
350 number of UAV photos. It increased rapidly as the number of the UAV photos number increased from 1 to 4 (from 0.74 to
351 0.86), then slowed down and stabilized (from 0.87 to 0.88). In addition, we compared the scatter plots and fitting lines
352 between NDVI and different AGB estimation methods (Figure 7b-f). The results showed a weak linear relationship between
353 the traditionally field-measured AGB and NDVI, with an R² of 0.29. With While the using the UAV sampling method, the
354 linear relationship was greatly improved and increased with the increasing the number of photographs photos. The fit
355 coefficient R² increased from 0.54 to 0.78, much higher than the traditional sampling method (Figure 7).

356

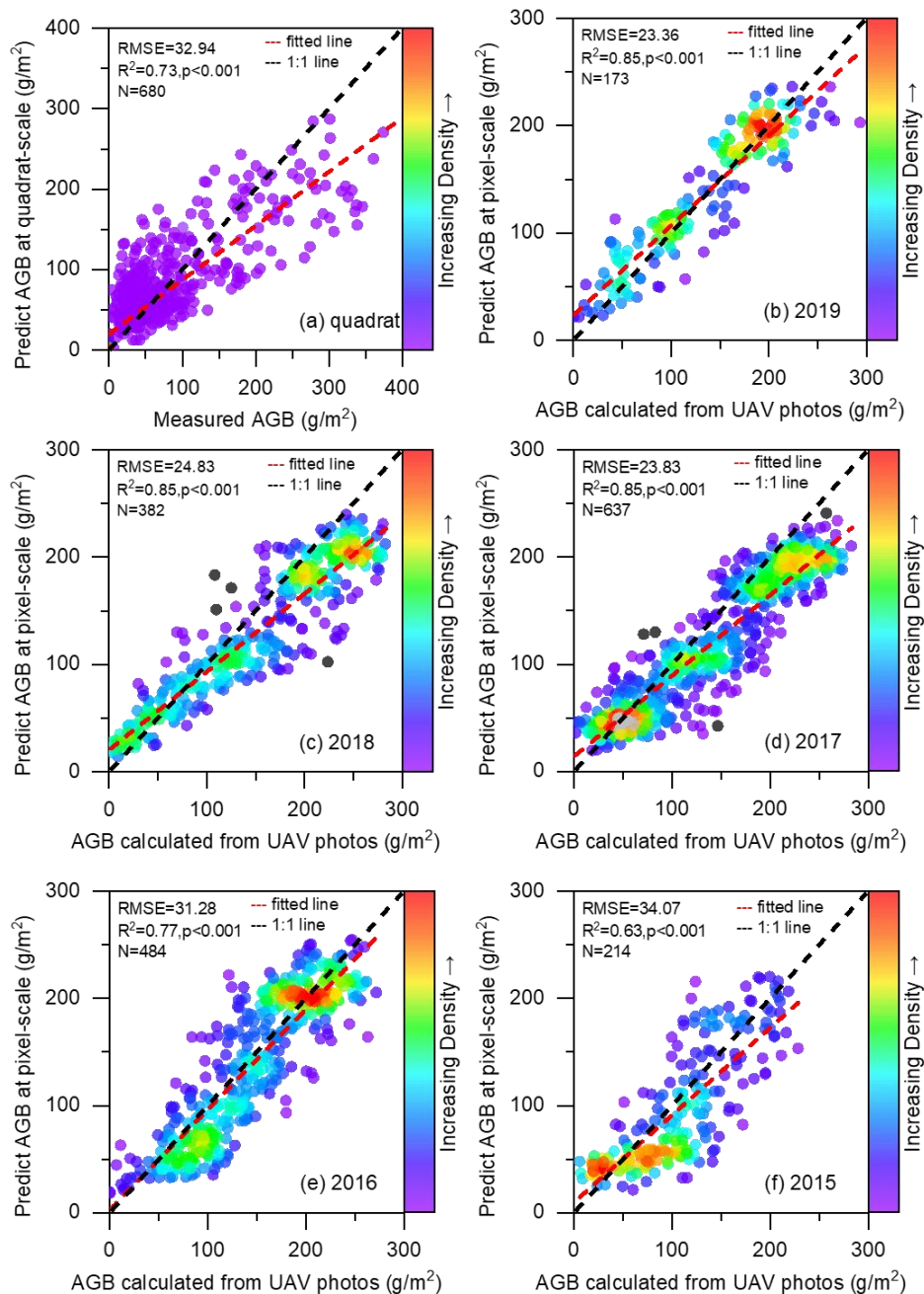
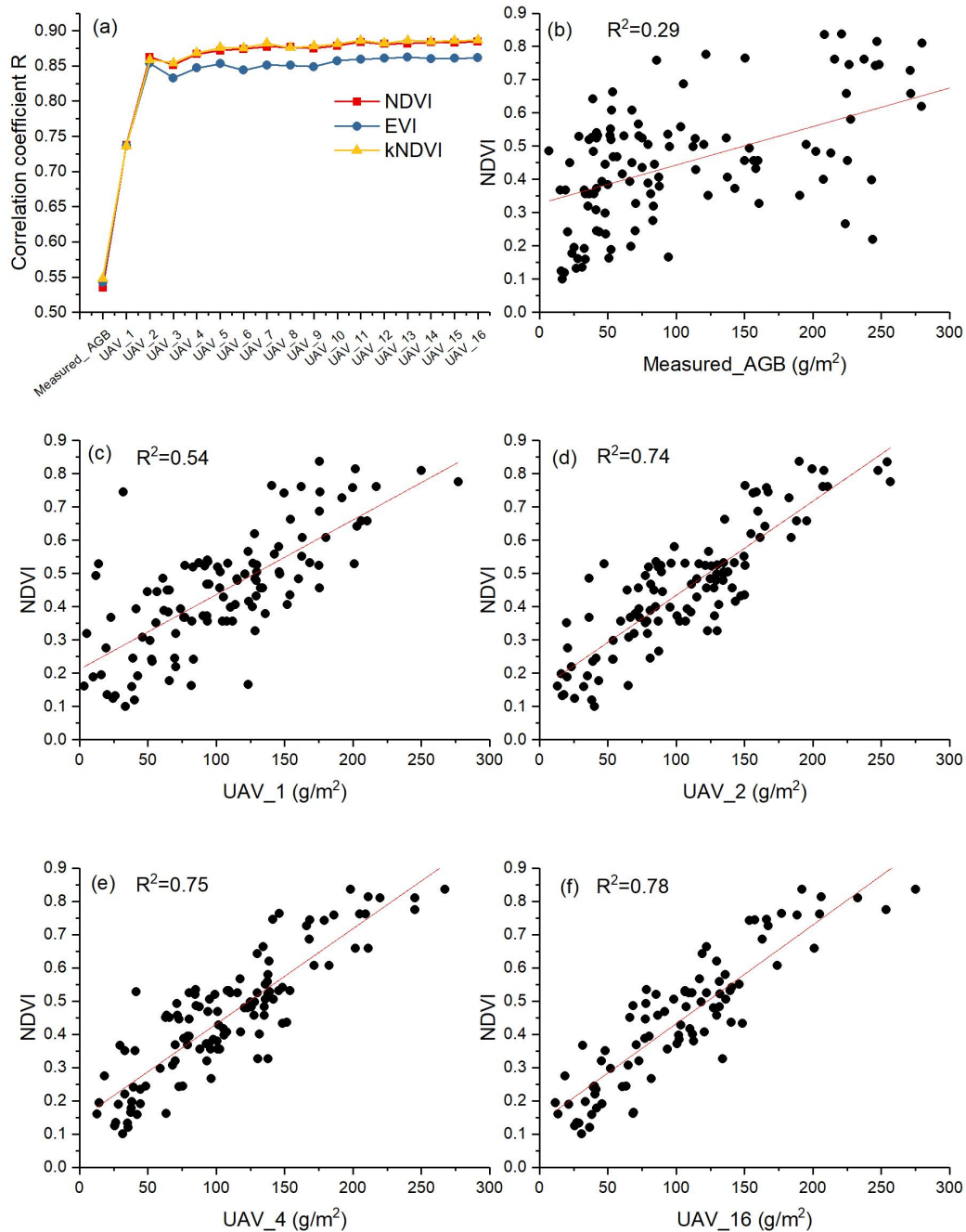


Figure 6. Validation results of the AGB estimation models at the quadrat (a) and MODIS pixel scale for 2015-2019 (b-f).



363
 364 **Figure 7. Correlation between MODIS vegetation indices and different AGB estimation methods (a); scatter plots of NDVI with**
 365 **different AGB estimation methods (b-f). UAV_x, x represents the number of UAV photos used to estimate the average AGB at the**
 366 **MODIS pixel scale. Here, x ranges from 1 to 16.**

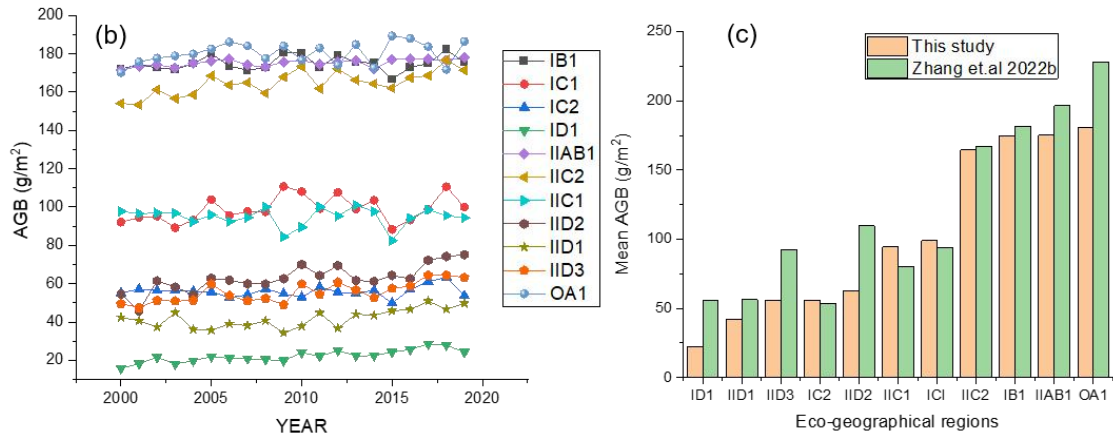
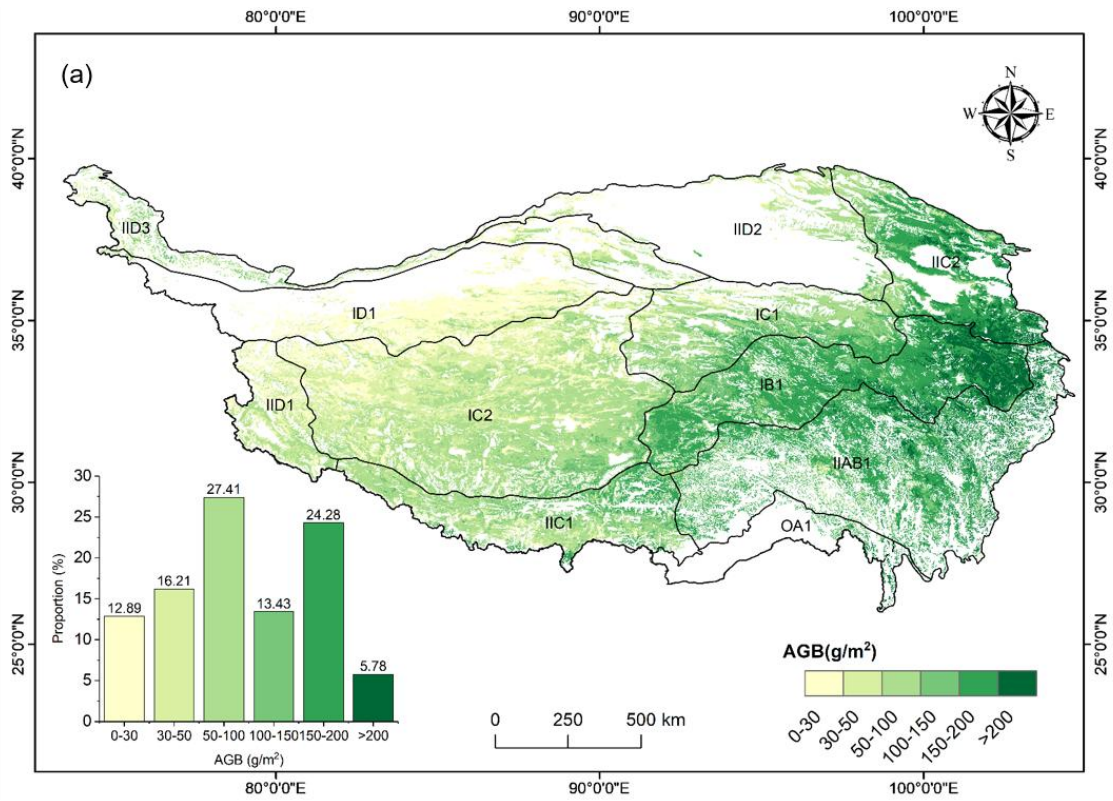
367

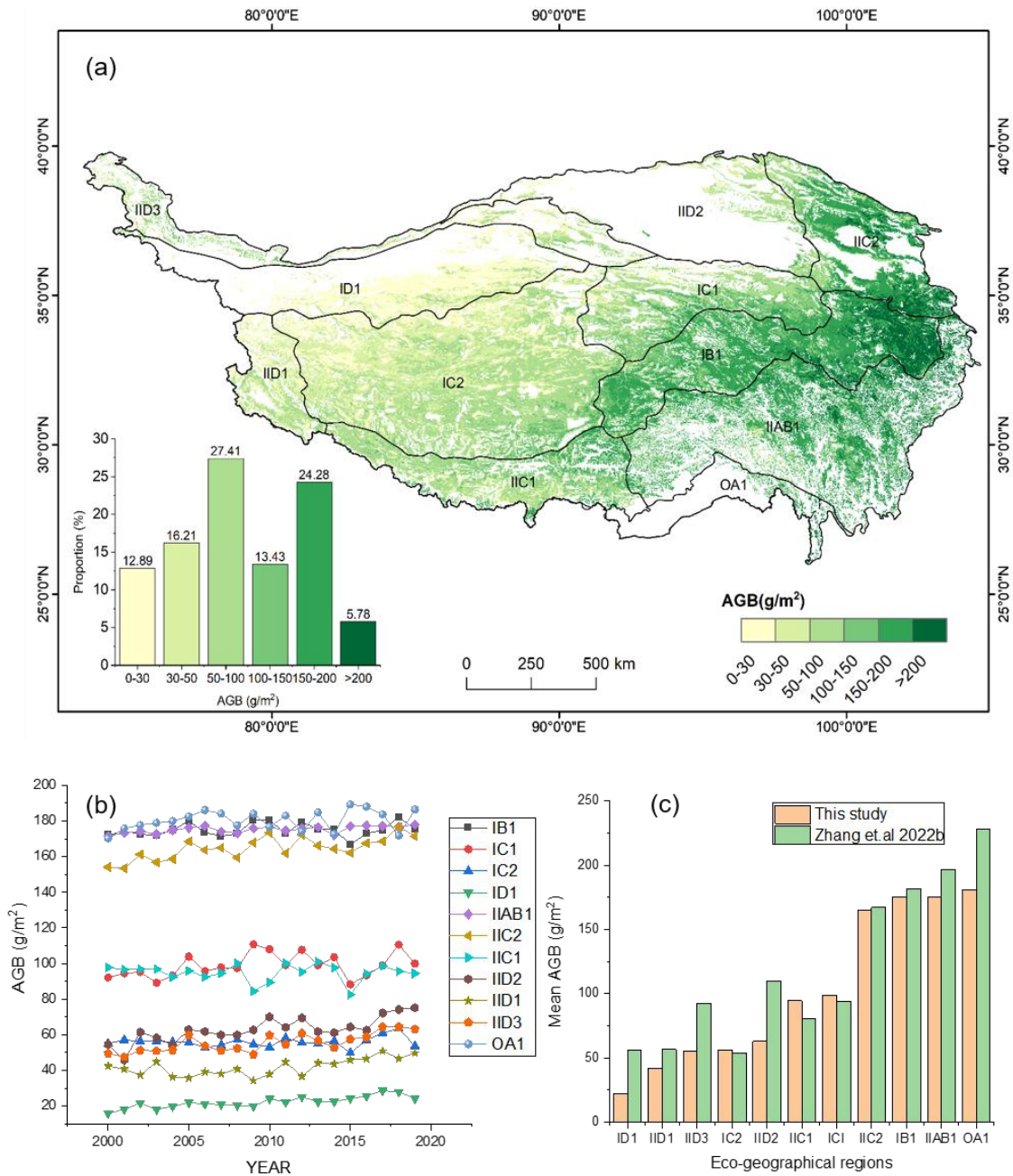
369 3.4 Spatial distribution of grassland AGB

370 The spatial distribution of the average grassland AGB on the QTP from 2000 to 2019 was calculated (Figure 8). The AGB
 371 gradually increased from west to east. ~~As shown in Figure 8b,~~ the average ~~AGB biomass~~ of eastern OA1, IIAB1, IB1, and
 372 IIC2 eco-geographical regions ranged from 150 to 190 $\text{g}\cdot\text{m}^{-2}\text{g}/\text{m}^2$, and the average AGB of IC1 and IIC1 ranged from 80 to
 373 110 $\text{g}\cdot\text{m}^{-2}$ (Figure 8b). The average AGB of IID2, IID3, IC2, and IID1 in the west was relatively low, ranging
 374 from 35 to 75 $\text{g}\cdot\text{m}^{-2}\text{g}/\text{m}^2$. The ID1 region was dominated by ~~sparse-desert~~ grassland with the lowest average ~~annual~~
 375 ~~interannual~~ AGB values, which fluctuated around 20 $\text{g}\cdot\text{m}^{-2}\text{g}/\text{m}^2$ (Figure 8b). ~~Except for the low AGB due to low~~
 376 ~~precipitation in 2015 (Figure A4), the mean AGB showed an overall increasing trend from 2000 to 2019, with an average~~
 377 ~~growth rate of 0.22 $\text{g}\cdot\text{m}^{-2}\cdot\text{a}^{-1}$ (Figure 9a). The average AGB of QTP showed an insignificant increasing trend between 2000~~
 378 ~~and 2019, with an average growth rate of 0.22 $\text{g}\cdot\text{m}^{-2}\text{a}^{-1}$ (Figure 9a).~~ The overall mean AGB of the QTP was 103.6 $\text{g}\cdot\text{m}^{-2}\text{g}/\text{m}^2$,
 379 with 151.85 $\text{g}\cdot\text{m}^{-2}\text{g}/\text{m}^2$, 60.85 $\text{g}\cdot\text{m}^{-2}\text{g}/\text{m}^2$, and 28.91 $\text{g}\cdot\text{m}^{-2}\text{g}/\text{m}^2$ for ~~alpine~~ meadow, ~~alpine~~ steppe, and ~~sparse-desert~~ grassland,
 380 respectively (Figure 9b). In addition, the temporal trend of grassland AGB in each pixel was analyzed. As shown in Figure
 381 10, the IID3, ID1, IID2, and IIC2 eco-geographical regions of the northern QTP showed an increasing trend from 2000 to
 382 2019, while the IC2, IB1, and IIC1 regions showed ~~some a degradation~~ ~~decreasing trend~~. Therefore, there was spatial
 383 heterogeneity in the temporal variation.

384

385



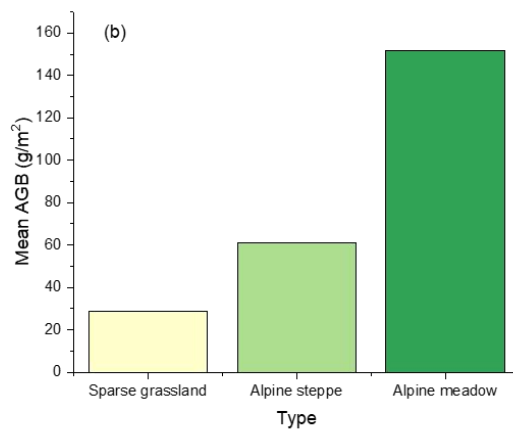
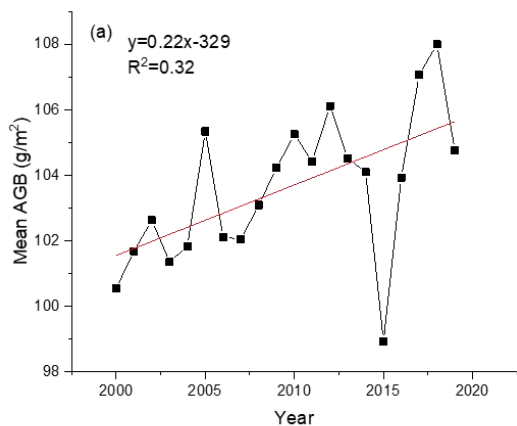


387

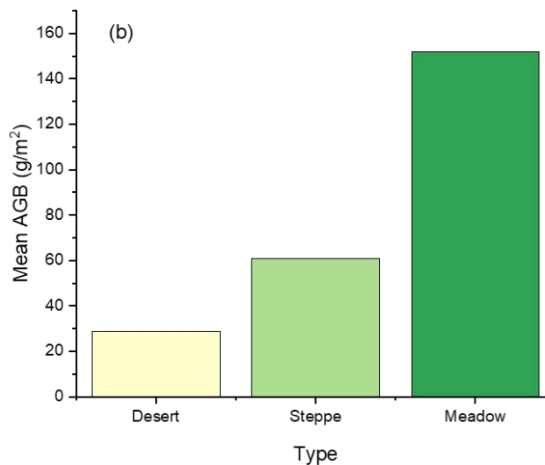
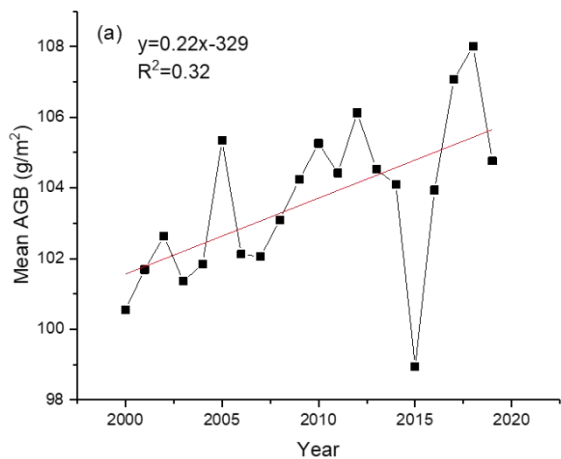
388

389 **Figure 8. (a) The spatial distribution of average grassland AGB on the QTP from 2000 to 2019. IID1, IID2, IID3, ID, IIC1, IIC2,**
 390 **IC1, IB1 IIB1, and OA1 are the eco-geographical regions of the QTP(Zheng, 1996). The full names of each eco-geographical**
 391 **region were listed in Table A5. (b) AGB values of each eco-geographical region from 2000 to 2019. (c) Comparison of multi-year**
 392 **AGB averages in the different eco-geographical regions.**

393

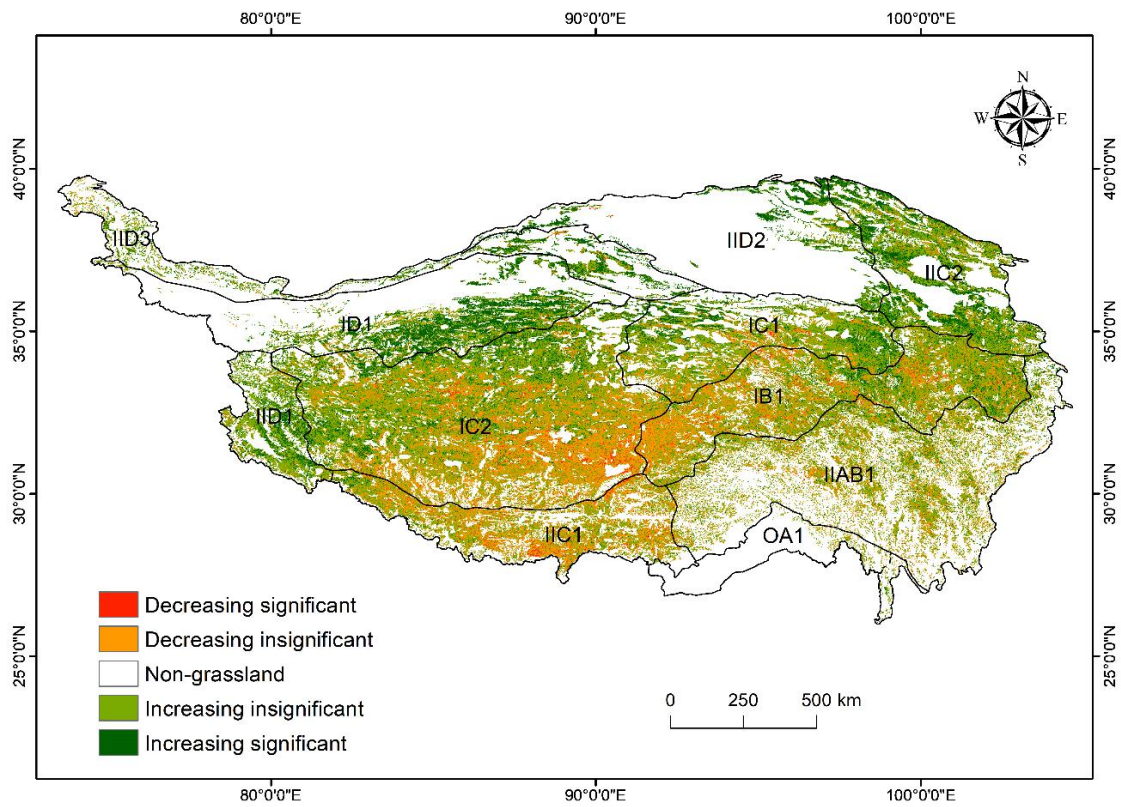


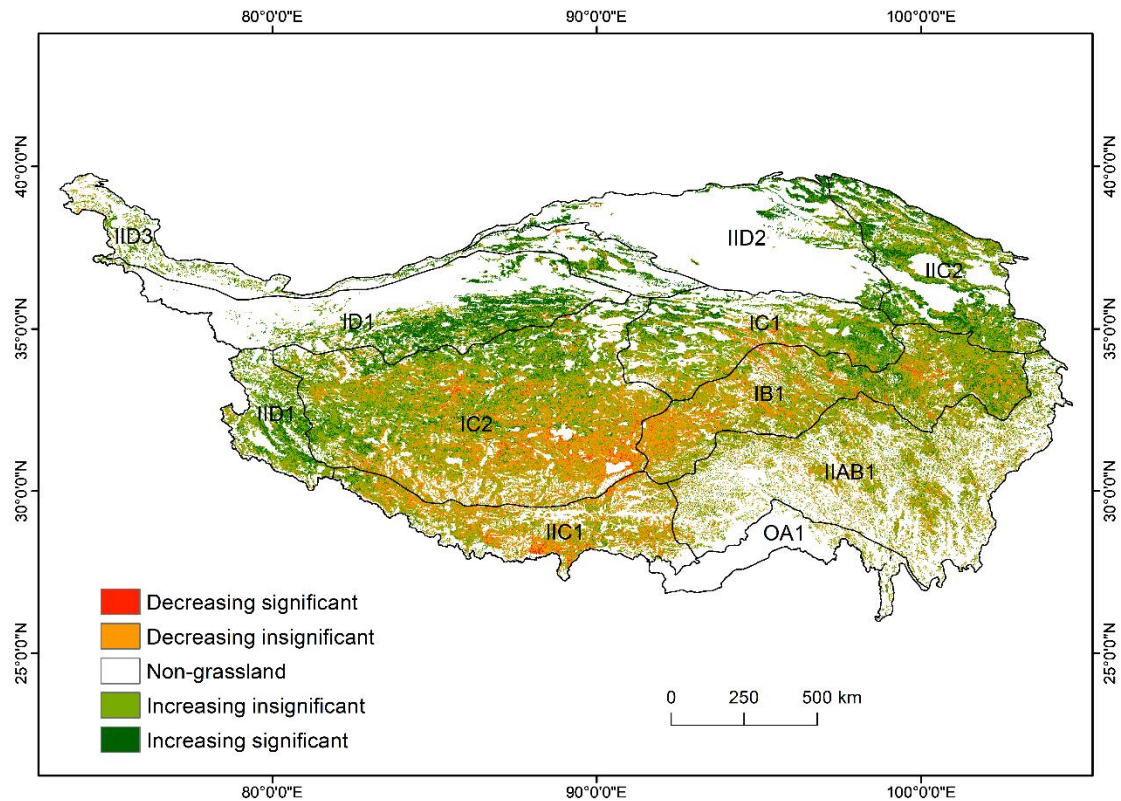
394



395

396 **Figure 9. Variation trend of average grassland AGB on the QTP from 2000 to 2019 (a) and average AGB of different grassland**
 397 **types (b).**





399

400 **Figure 10. Spatial trends of grassland AGB on the QTP from 2000 to 2019. IID1, IID2, IID3, ID1, IIC1, IIC2, IC1, IB1 IIAB1, and**
 401 **OA1 are the eco-geographical regions of the QTP (Zheng, 1996). The full names of each eco-geographical region were listed in**
 402 **Table A5.**

403

404

405 4 Discussion

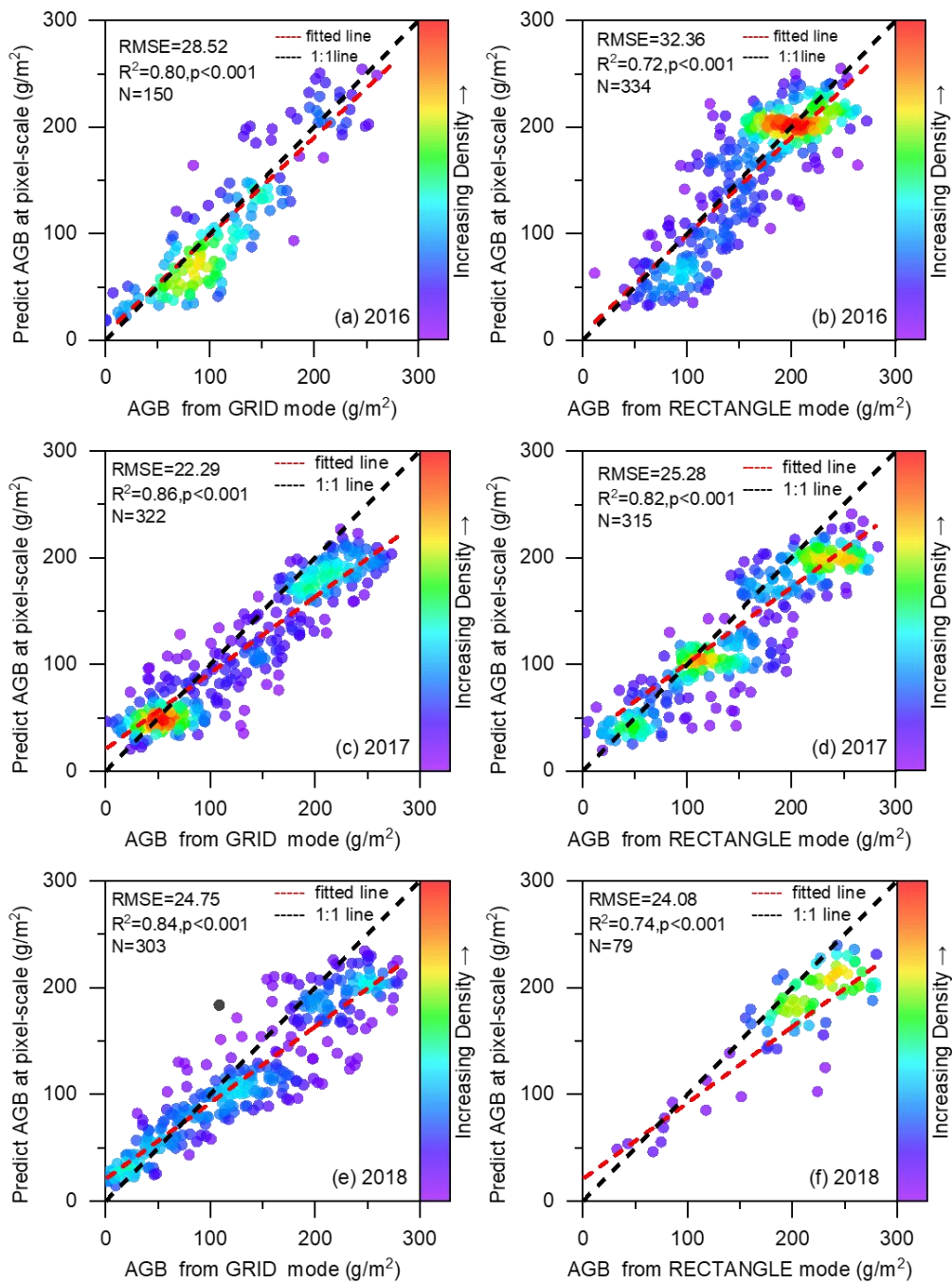
406 4.1 Scale matching and its **impact influence** factor

407 In previous studies, the AGB values at the a-satellite pixel scale were usually represented by the average of 3-5 quadrat-
 408 scale samples placed in the corresponding satellite pixel, resulting in ~~so there is~~ a large spatial gap between the ground
 409 samples and the satellite pixels (Yang et al., 2017; Yang et al., 2009; Meng et al., 2020). ~~The spatial gap between ground~~
 410 samples and satellite ~~indices-pixels~~ affects the accuracy of grassland AGB inversion-estimation models. ~~The smaller the~~
 411 ~~spatial gap between the two, the higher the accuracy of the model.~~ (Morais et al., 2021). ~~Therefore, we~~ addressed this
 412 issue using the UAVs as a bridge to reduce-fill the spatial gap. Spatial scale matching of dependent and independent
 413 variables was achieved in estimating AGB values at different scales. ~~Firstly~~, at the quadrat scale, the independent variables

414 were all derived from cropped 20-meter-high UAV ~~images-photos~~ corresponding to the ground samples (Figure 3e). ~~Then~~
415 ~~Secondly~~, the 20-meter-high UAV ~~image-photo~~ was ~~cropped-split~~ into ~2000 quadrat-sized patches to ensure consistency
416 with the quadrat-scale model, and the average of these patches was used as the final AGB at the photo scale. ~~Finally~~, ~~by~~
417 ~~averaging the AGB of 16 or 12 UAV photos within the MODIS pixel~~, the AGB ~~value~~-matching the MODIS pixel scale was
418 calculated ~~by averaging the AGB of 16 or 12 UAV photos within the MODIS pixel~~ (Figure A1). With these three steps, we
419 successfully upscaled the measured AGB from ~~the traditional~~-quadrat scale (0.5 m \times 0.5 m) to ~~the~~-photo scale (26 m \times 35 m)
420 and MODIS pixel scale (250 m \times 250 m). Our results showed that the correlations between the UAV-estimated AGB values
421 and the MODIS vegetation indices were higher than that ~~between field harvested AGB and MODIS vegetation indices of the~~
422 ~~traditional sampling method~~ (Figure 7).

423

424 Furthermore, we found that the spatial coverage ~~area~~ of the UAV sampling had an impact on the scale matching. Our results
425 showed that the closer the spatial coverage ~~area~~ of the UAV sampling was to the satellite pixel, the higher its correlation with
426 MODIS ~~vegetationspectral~~ indices (Figure 7a). It was ~~also further~~ confirmed by comparing the validation results of different
427 flight modes. At the ~~MODIS~~ pixel scale, we found that the R^2 between the model predictions and the AGB values estimated
428 ~~based on the by~~ GRID mode was better than that of ~~the~~-RECTANGLE ~~mode~~ (Figure 11). The reason is that ~~the~~-GIRD mode
429 can take 16 ~~pictures-photos~~ within a MODIS pixel, while ~~the~~-RECTANGLE mode ~~can~~ only takes 12 ~~pictures-photos~~ (Figure
430 A1). ~~The above results confirmed that~~ ~~As a result~~, UAV ~~photos s~~-could serve as a bridge to effectively ~~reduce-fill~~ the spatial
431 gap between traditional samples and satellite data.



432

433 **Figure 11. Comparison of validation results for the GRID (a,c,e) and RECTANGLE (b,d,f) modes in 2016-2018.**

434 4.2 Importance of the addition of non-vegetation samples

435 Compared with traditional sampling (Yang et al., 2017), UAV sampling has ~~the-the~~ advantage of ~~wide-larger~~ spatial
436 coverage ~~area~~ (0.5 m × 0.5 m vs. 35 m × 26 m). Thus, the UAV ~~photo image~~ could capture ~~vegetation and~~ non-vegetation
437 background information, such as roads, water, soil, gravel, and riverbed ~~,~~ (Figure A54). Adding non-vegetation samples
438 could improve the accuracy of AGB estimation at the photo scale, especially for ~~areas with low vegetation coverlow cover~~
439 ~~areas, to avoid overestimation~~. It was also ~~suitable true~~ for the pixel-scale AGB estimation model. ~~However, the traditional~~
440 ~~sampling method gave less consideration to the non-vegetation areas. The sample plots were mainly set in areas with~~
441 ~~homogeneous spatial distribution, and rarely in areas with spatial heterogeneity. This shortcoming may limit the accuracy of~~
442 ~~AGB estimation due to the high spatial heterogeneity of the QTP. Fortunately, the UAV sampling method can objectively~~
443 ~~record surface information and reduce the influence of manual plot selection on AGB estimation.~~

444 4.3 Comparison of the estimated AGB with previous studies

445 We compared our results with previous studies at the quadrat, pixel, and regional scales.

446
447 At the quadrat scale, consistent with our previous study, we further confirmed that the UAV ~~RGB images-photos~~ could be
448 used to estimate grassland AGB (Zhang et al., 2022a; Zhang et al., 2018). ~~Similar to the 2-meter-high UAV imagephoto, the~~
449 ~~indices from~~ the 20-meter-high UAV ~~photo image~~ could be used to estimate the grassland AGB at the quadrat scale ($R^2 =$
450 0.73 , $RMSE = 44.23 \text{ g} \cdot \text{m}^{-2} / \text{g} \cdot \text{m}^{-2}$, Figure 6a). ~~Compared with the 2-meter-high UAV photo (0.8 m × 1 m)image, the 20-~~
451 ~~meter-high UAV photo (26 m × 35 m) image~~ is more suitable for matching the MODIS pixel due to its ~~wider-larger~~ spatial
452 coverage ~~area (26 m 35 m)~~. ~~In addition, the direct use of the 20-meter-high photo eliminates the need for spatial scale~~
453 ~~conversions when upscaling the AGB estimation from the quadrat scale to the photo scale.~~

454
455 At the pixel scale, compared with other studies, this paper achieved the spatial scale matching of independent and dependent
456 variables during the modeling. ~~In previous studies (Yang et al., 2009; Yang et al., 2017; Meng et al., 2020), they~~
457 ~~constructed the models from the measured AGB values at the quadrat scale and the spectral indices of the satellites without~~
458 ~~considering the spatial scale difference. It partly explained why the R^2 of the AGB linear model constructed by Yang et al.~~
459 ~~(2009) was only 0.4 (Yang et al., 2009). Our results confirmed that the R^2 of the linear model could be increased from 0.29~~
460 ~~to 0.78 after filling reduceing~~ the spatial gap between measured AGB and MODIS NDVI (Figure 7). In addition, thanks to the
461 rapid sampling of UAV ~~technology~~ AGB, a total of 2,602 ~~UAV samples~~ matching the ~~MODIS~~ pixel scale were collected
462 during 2015-2019. It allowed us to perform ~~eross~~ multi-year validation to assess the robustness of the model over time, which
463 has rarely been performed in previous studies. Our results showed similar validation results for 2017-2019, ~~($R^2 = 0.85$,~~
464 ~~$p < 0.001$)~~ despite different sample ~~amounts~~ sizes and spatial distributions (Figure 1, Table 1). But in 2015-2016, R^2 was
465 relatively low, at 0.63 and 0.77, respectively (Table 3, Figure 6). The reason was that during 2015-2016, some photos with

466 ~~abnormal-unnatural~~ white balance were obtained due to improper settings, which reduced the estimation accuracy (Figure
 467 A65). The validation results showed that the MODIS pixel-scale AGB estimation model had good robustness in different
 468 regions and times when ~~ever~~ the ~~photo-quality~~ photo quality -was acceptable.

469

470 ~~At the regional scale, consistent with previous results, we found an overall increase in AGB over the QTP from 2004 to~~
 471 ~~2019, albeit with fluctuations (Zeng et al., 2019; Gao et al., 2020). The annual average AGB of grassland was 103.6 g·m⁻²,~~
 472 ~~which was closest to Zhang et al.(2022b) and within the range of the previous estimates (59.63-120.73 g·m⁻²) (Table 5). The~~
 473 ~~mean~~

474 **Table 5: Comparison of AGB estimation results of different studies on the QTP**

Mean AGB (g/m ²)	Alpine steppe (g/m ²)	Alpine meadow (g/m ²)	Study period	Approach	Input parameter	References
68.8	50.1	90.8	2001-2004	Linear regression	EVI	(Yang et al., 2009)
==	22.4	42.37	2000-2012	Linear regression	NDVI	(Liu et al., 2017)
120.73	==	==	1980-2014	Exponential regression	NDVI	(Jiao et al., 2017)
78.4	==	==	1982-2010	RF	NDVI, climate	(Xia et al., 2018)
77.12	76.43	154.72	2000-2014	RF	NDVI, EVI, climate, terrain	(Zeng et al., 2019)
59.63	42.75	77.56	2000-2017	RF	NDVI, climate	(Gao et al., 2020)
102.4	==	==	2000-2020	RF	climate, soil, and terrain	(Zhang et al., 2022b)
70.00	==	==	1960-2002	Century	climate and soil data	(Zhang et al., 2007)
119.78	==	==	2002-2004	Orchidee	climate, soil and LAI data	(Tan et al., 2010)
103.6	60.85	151.85	2000-2019	RF	MODIS	this study

475

476 ~~AGB~~ ~~At the regional scale, consistent with previous results, we found an overall increase in AGB over the QTP from~~
 477 ~~2001 to 2019, albeit with fluctuations (Zeng et al., 2019; Gao et al., 2020). The annual average AGB of grassland was~~
 478 ~~103.6 g/m², which was closest to Zhang et al.(Zhang et al., 2022b) and within the range of the previous estimates (59.63-~~
 479 ~~120.73 g/m²) (Table 5). The mean AGB varied among different grassland types, with 151.85 g·m⁻²/g/m² for the alpine~~
 480 ~~meadow and 60.85 g·m⁻²/g/m² for the alpine steppe. Our estimation results were similar to those of Zeng et al.(2019)(Zeng et~~
 481 ~~al., 2019), but the overall average AGB was higher than their estimate of 77.12 g·m⁻²/g/m². The spatial distribution of AGB~~
 482 ~~was consistent with previous studies, showing a west-to-east increasing trend (Zhang et al., 2022b; Xia et al., 2018).~~
 483 ~~Specifically, the average AGB of OA1, IIAB1, IB1, and IIC2 eco-geographical regions in the east was significantly higher~~
 484 ~~than that of IID2, IID3, IC2, IID1, and ID1 regions in the west (Figure 8). In general, the average AGB estimates for each~~
 485 ~~eco-geographical region in this paper were similar to those reported not much different from by those of Zhang et al. (2022b).~~
 486 ~~Among them, our average AGB estimates for ID1, IID1, IID3, and IID2 regions were slightly lower, but our values were~~

487 closer to the measured values of these regions (Figure 8c). The reason may be that they calculated the potential AGB, while
 488 we calculated the actual AGB, so our estimate was relatively low. In terms of spatial and temporal trends, the data results
 489 showed that the eco-geographical regions in the northern part of the QTP demonstrated an increasing trend (IID3, ID1, IID2,
 490 and IIC2), while the IC2, IIC1, and IB1 regions exhibited significant or non-significant decrease, which was consistent with
 491 the results of others (Gao et al., 2020; Liu et al., 2017).

492

493 **Table 5. Comparison of AGB estimation results of different studies on the QTP**

<u>Mean AGB</u> <u>(g·m⁻²)</u>	<u>Steppe</u> <u>(g·m⁻²)</u>	<u>Meadow</u> <u>(g·m⁻²)</u>	<u>Study period</u>	<u>Approach</u>	<u>Input parameter</u>	<u>References</u>
68.8	50.1	90.8	2001-2004	Linear regression	EVI	(Yang et al., 2009)
—	22.4	42.37	2000-2012	Linear regression	NDVI	(Liu et al., 2017)
120.73	—	—	1980-2014	Exponential regression	NDVI	(Jiao et al., 2017)
78.4	—	—	1982-2010	RF	NDVI, climate	(Xia et al., 2018)
77.12	76.43	154.72	2000-2014	RF	NDVI, EVI, climate, terrain	(Zeng et al., 2019)
59.63	42.75	77.56	2000-2017	RF	NDVI, climate	(Gao et al., 2020)
102.4	—	—	2000-2020	RF	climate, soil, and terrain	(Zhang et al., 2022b)
70.00	—	—	1960-2002	Century	climate and soil data	(Zhang et al., 2007)
119.78	—	—	2002-2004	Orchidee	climate, soil and LAI data	(Tan et al., 2010)
103.6	60.85	151.85	2000-2019	RF	MODIS	this study

494

495

496 The difference between our estimated grassland AGB and previous studies might be due to differences in data sources and
 497 modeling methods. — Firstly, the sample ~~size~~ amount and spatial distribution of ground samples were different. The number
 498 of ground samples is the most important variable affecting the accuracy of the grassland AGB estimation model (Morais et
 499 al., 2021). Unlike previous studies, we collected ground validation data by combining the traditional sampling method and
 500 UAVs. The newly proposed method could overcome the shortcomings of traditional samplings (time-consuming and labor-
 501 intensive). It no longer takes years to obtain spatially representative, large-scale ground validation data (Yang et al., 2017).
 502 With UAV sampling, ground observations matching the satellite pixel scale can be obtained in only 15-20 minutes, which is
 503 difficult to achieve in traditional surveys. Our new sampling method not only accelerates the sampling speed and increases
 504 the sample ~~amount~~ size, but also improves the spatial match between ground samples and satellite pixels. As a result, our
 505 ground validation data is ~~superior~~ better to than previous studies in terms of quantity and spatial ~~scale~~ -matching with ~~to~~ the
 506 satellite data. Secondly, the input parameters of AGB estimation models were different. Some scholars used only a single
 507 vegetation index (NDVI or EVI), while others combined the vegetation index with meteorological, soil, and terrain indices to
 508 construct the AGB estimation models (Table 5). In this study, NDVI, kNDVI, EVI, DEM, and ~~PREC~~ MAP were used as the

509 final predictor variables to construct the AGB estimation model at the [MODIS](#) pixel scale (Table 2). Thirdly, modeling
510 methods might also affect the [simulation-estimation](#) results. As shown in Table 5, the overall AGB averages of the QTP
511 estimated based on different methods (such as linear or nonlinear regression, machine learning, and ecological process model
512 methods) varied considerably. Yang et al. (2017) found that the model performance ~~of the artificial neural network (ANN)~~
513 was much better than the linear regression model when using the same dataset to estimate grassland AGB in the Three-River
514 Headwaters Region of China. Jia et al. (2016) reported that the model forms could bring -13% uncertainty to the AGB
515 estimation. Wang et al. (2017) compared the RF with the [bagging, mboost, and](#) support vector regression (SVR) ~~machine-~~
516 ~~learning~~ algorithms, and found that the RF yielded ~~the the best-best~~ performance in grassland ~~biomass-AGB~~ estimation.
517 ~~(Wang et al., 2017).~~

518

519 4.4 Limitations and further work

520 We acknowledge that there are some shortcomings in this study. 1) The predicted values of the quadrat-scale model were
521 underestimated when the measured biomass values were greater than $250 \text{ g}\cdot\text{m}^{-2}\text{g}/\text{m}^2$ (Figure 6). ~~One of the reasons may be~~
522 ~~that the number of samples larger than $250 \text{ g}\cdot\text{m}^{-2}$ at the quadrat scale is relatively small, accounting for only 5.18% of the~~
523 ~~total samples. Another possible reason is that the height of the grassland could not be detected by a single UAV photo.~~
524 ~~Therefore, it could lead to an underestimation of AGB for grassland species with the same FVC but greater heights. One~~
525 ~~reason may be that the number of samples greater than $250 \text{ g}/\text{m}^2$ was relatively small, accounting for only 5.18 % of all~~
526 ~~samples. Another reason may be that for high biomass grasslands, a single UAV RGB photo can only reflect information~~
527 ~~such as vegetation cover and greenness, but not height information. This feature is very unfavorable for estimating AGB in~~
528 ~~grassland areas with high vegetation coverage and height. Previous s~~Studies have shown that adding vegetation height
529 information can ~~help~~ improve the estimation accuracy of grassland AGB (Zhang et al., 2022a; Lussem et al., 2019; Viljanen
530 et al., 2018). In future work, an affordable DJI Zensil L1 Lidar UAV will be introduced to ~~invert-detect~~ the height of the
531 grassland. 2) At the [MODIS](#) pixel scale, limited by the estimation accuracy of AGB from UAV ~~photos~~, there was also some
532 underestimation in the high biomass area. Although the MODIS ~~indices~~index closest to the sampling ~~time-date was-were~~
533 chosen for the construction/validation of the AGB estimation model, there was still a time ~~gap difference~~ between the
534 measured samples and the MODIS indices, which might lead to estimation ~~uncertainties~~errors. In addition, the NDVI
535 saturation problem was not considered in this study, which might affect the AGB estimation accuracy ~~in of~~ QTP (Tucker,
536 1979a; Gao et al., 2000; Mutanga and Skidmore, 2004; Tucker, 1979b). In the next step, we will continue to collect samples
537 with high biomass and try to correct the NDVI saturation problem ~~forte~~-optimizeing the simulation accuracy of the data-set.
538 3) During 2015-2016, ~~we set the automatic white balance mode for UAV shooting due to inexperience our study had just~~
539 ~~started, and the appropriate camera parameters were still being explored.~~ As a result, some photos with ~~abnormal-unnatural~~
540 white balance were obtained, reducing the accuracy of AGB estimation at the photo scale (Figure [A5A6](#)). -4) We collected
541 grassland AGB only during the peak growing season, and the applicability of the proposed method to other growing seasons

542 needs further study. 5) During the modeling process, due to the ~~poor limited~~-positioning accuracy, only the center points of
543 the flight path were used to find the corresponding MODIS pixels. Moreover, although the UAV ~~photos images~~-in GRID or
544 RECTANGLE mode could cover most areas of a MODIS pixel, full pixel coverage was still not achieved. Therefore, we will
545 gradually upscale to MODIS pixels by combining UAVs with Sentinel-2 or Landsat images.

546

547 **5 Data availability**

548 The dataset is available from the National Tibetan Plateau/Third Pole Environment Data Center
549 (<https://doi.org/10.11888/Terre.tpd.272587>). The dataset contains 20 years of AGB spatial data of the QTP with a resolution
550 of 250 m and is stored in TIFF format. The name of the file is "AGB_YYYY.tif", where YYYY represents the year. For example,
551 AGB_2000.tif represents this TIFF file describing the alpine grassland AGB condition of QTP in 2000. The data can be
552 readily imported into standard geographical information system software (e.g., ArcGIS) or accessed programmatically (e.g.,
553 MATLAB, Python).

554 **6 Conclusion**

555 ~~T~~-In this study ~~developed~~, a new AGB dataset for alpine grasslands on the QTP ~~was calculated~~-based on traditional ground
556 sampling, UAV photography, and MODIS imagery. The uniqueness of this dataset is the use of UAVs as a spatial scale-
557 matching bridge between traditional samples and ~~satellite-MODIS~~ pixels. The study confirmed that the UAV ~~photos images~~-
558 could be used for AGB estimation at the quadrat-/MODIS pixel scale, with R^2 of 0.73/0.83 and RMSE of 44.23/34.13 ~~g·m~~
559 ~~²g/m²~~, respectively. At the MODIS pixel scale, the correlations between AGB estimated by UAV and MODIS vegetation
560 ~~indices index was were~~ higher than ~~that of the betweentraditional field harvested AGB and MODIS vegetation~~
561 ~~indicesampling methodthat of the traditional sampling method (0.88 vs. 0.53)~~. Moreover, the spatial scale matching of the
562 dependent and the independent variables was achieved during the modeling. In addition, we performed a ~~eross~~multi-year
563 validation of the MODIS pixel-scale AGB estimation model to confirm the robustness of the model and the accuracy of this
564 dataset. The availability of the new dataset is helpful in many applications. First, this dataset provides reliable regional data
565 for estimating grassland productivity, carbon storage, ecological carrying capacity, and ecological service functions (such
566 as feed for grazing livestock) of the QTP. Second, the dataset can be used to understand the mechanisms of environmental
567 processes, such as hydrological cycle processes, soil erosion and degradation, and carbon cycle processes in the QTP. In
568 addition, this dataset can be used as input or validation parameters for various ecological models to understand the response
569 mechanism of the QTP to global climate change.

570 **7 Author contributions**

571 HZ contributed to the study conceptualization, methodology, funding acquisition, and the original draft of the manuscript.
572 ZT, BW, and HK contributed to resources and formal analysis. ~~YQY~~ and YS contributed to data collection and manuscript
573 review. BM, ML, and JC contributed to the methodology and reviewed the manuscript. YL and JZ participated in reviewing
574 and editing the manuscript. SN contributed to the data collection and review of the manuscript. SY contributed to the study
575 conceptualization, funding acquisition, and manuscript review. All authors have read and approved the manuscript.

576 **8 Competing interests**

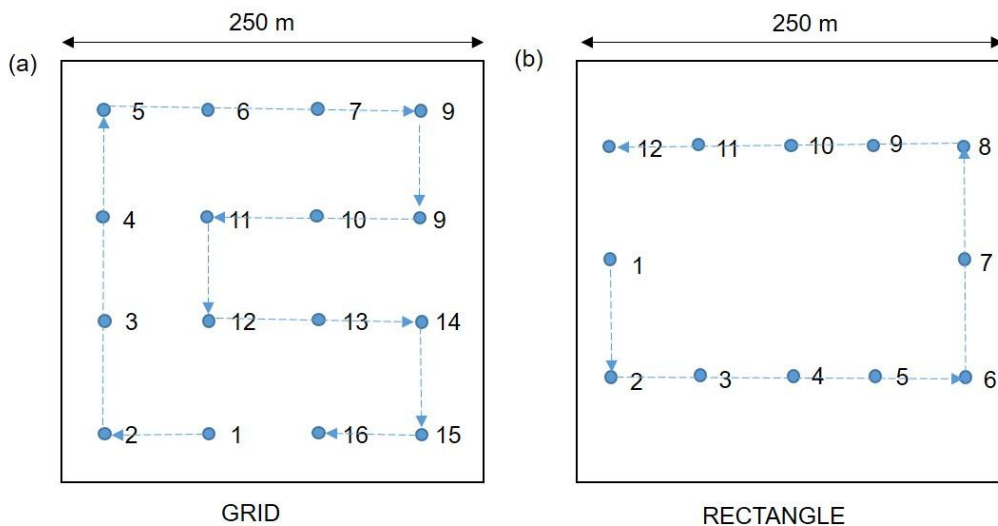
577 The authors declare that they have no conflict of interest.

578 **9 Acknowledgements**

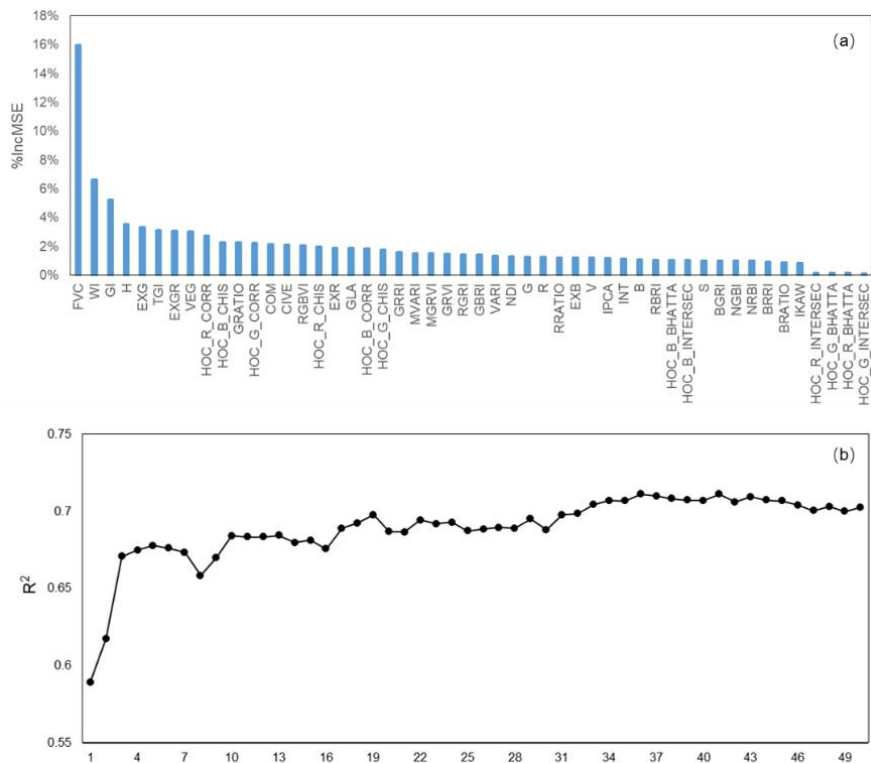
579 We would like to express our gratitude to the other students and staff who participated in the field investigation.

580 **10 Financial support**

581 This research was supported by the National Natural Science Foundation of China [grant nos: 41801023], the National Key
582 R&D Program of China [grant nos: 2017YFA0604801], and the National Natural Science Foundation of China [grant nos:
583 ~~418011024~~[2071056](#)].



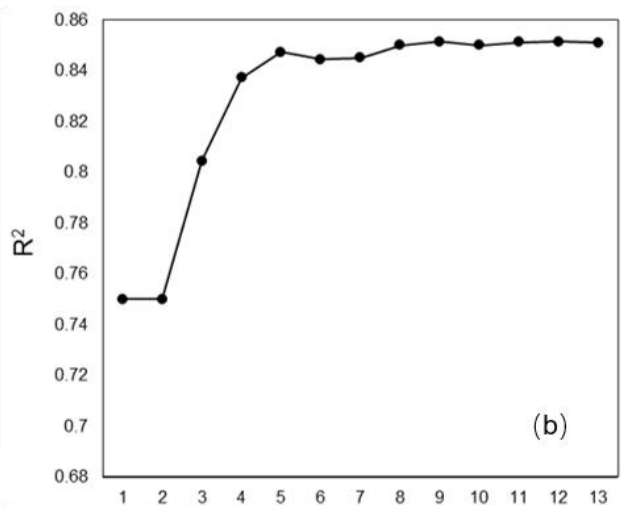
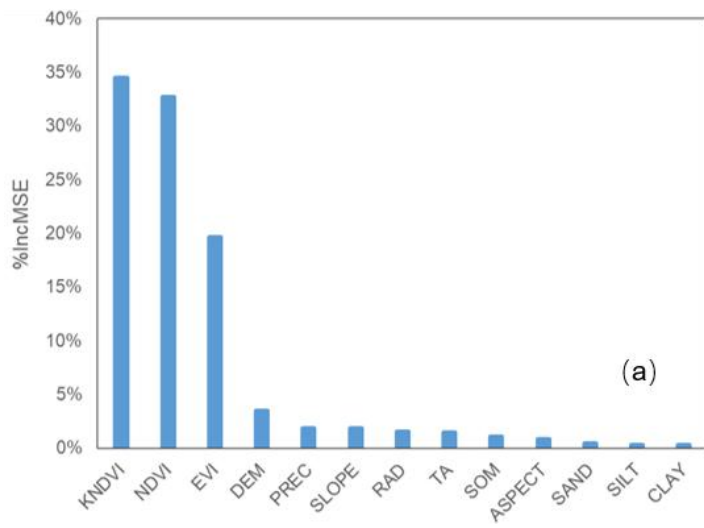
585
586 Figure A1. Waypoints for GRID (a) and RECTANGLE (b) flight modes.



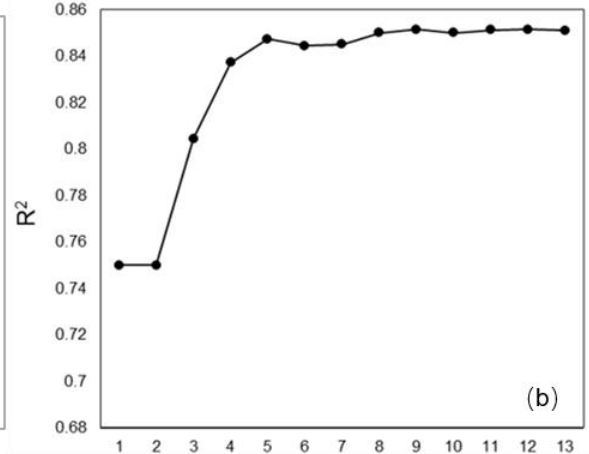
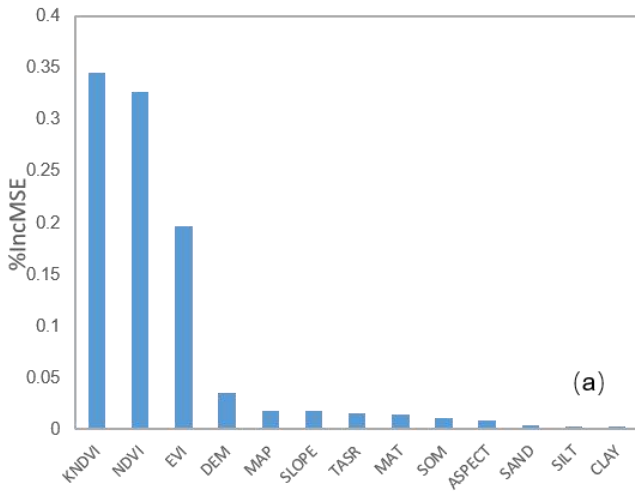
587
588 Figure A2. The importance values for each independent variable (a) and the R^2 results of the different number of input variables
589 at the quadrat scale.

590

591



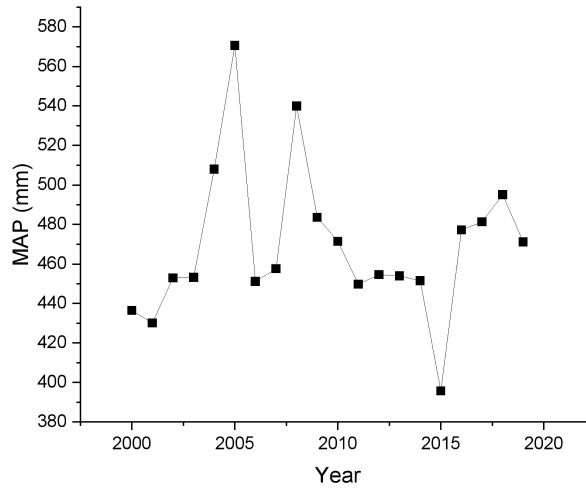
592



593

594

595 **Figure A3.** The importance values for each independent variable (a) and the R² results of the different number of input variables
596 at the **MODIS** pixel scale.

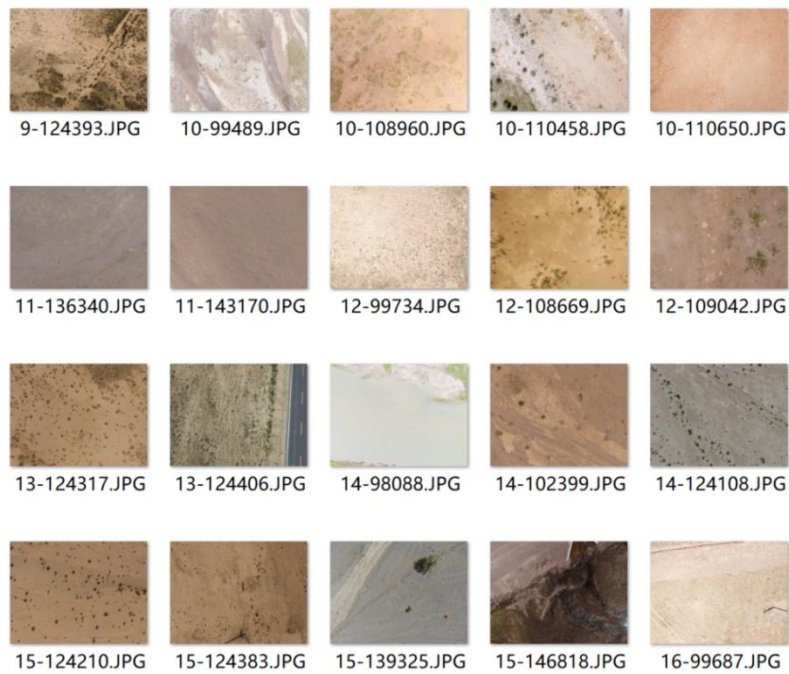


597

598

599

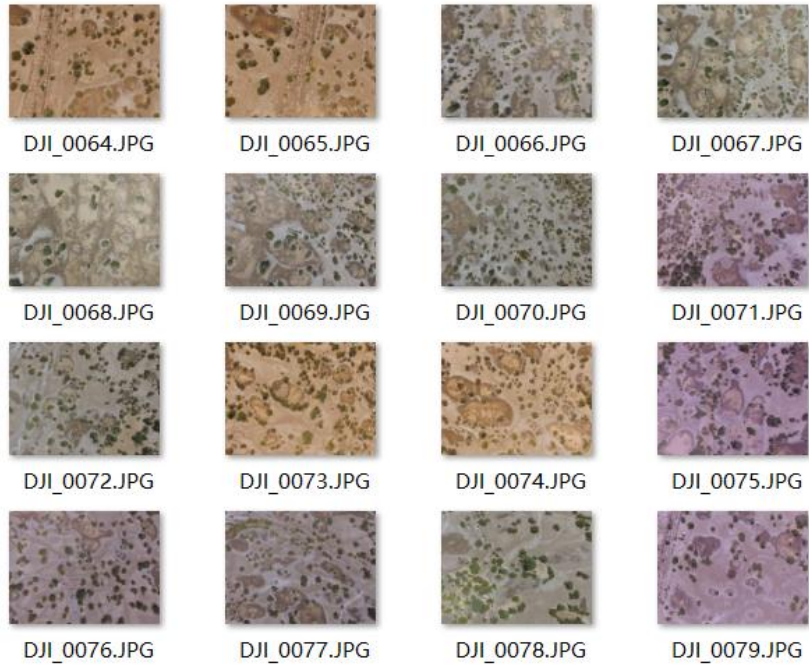
Figure A4. Mean annual precipitation (MAP) on the QTP from 2000-2019.



600

601

Figure A4A5. Examples of 20-meter-high UAV imagesphotos with different non-vegetation background information.



602
603 **Figure A5A6.** An example of a set of GIRD photos with unnatural abnormal-white balance in 2015.


604
605

606 **Table A1.** Combined grassland types

New grassland type	Original grassland type
Alpine-M meadow	Alpine meadow, Lowland meadow, Montane meadow,
Alpine-S steppe	Temperate steppe, Alpine steppe, Alpine meadow steppe
DesertS pare-grassland	Temperate steppe desert, Alpine desert

607
608
609

610 **Table A2.** Features of DJI Phantom 3 Pro

	Features	Description
	Sensor	1/23-inch; Effective-pixel: 12-megapixel
	Field of view	FOV 94° 20 mm
	Aperture	f/2.8

DJI Phantom 3 Pro	Shooting speed	Electronic shutter: 8-1/8000 s
	Photo size	4000×3000
	Flight time	~25 min
	Image format	JPEG
	Hovering accuracy	±0.5 m vertically; ±1.5 m horizontally
	Weight	1280 g

611

612

613

614

615 **Table A3** → **Details of the independent variables for quadrat-scale AGB estimation**

Acronym	Index name	Formula	Reference
GRVI	Green Red Vegetation Index	$(G-R)/(G+R)$	(Tucker, 1979a)
EXG	Excess Green Vegetation Index	$2G-R-B$	(Woebbecke et al., 1995)
GLA	Green leaf area	$(2G-R-B)/(2G+R+B)$	(Louhaichi et al.)
MGRVI	Modified Green Blue Vegetation Index	$(G2-R2)/(G2+R2)$	(Bendig et al., 2015)
RGBVI	Red Green Blue Vegetation Index	$(G2-B*R)/(G2+B*R)$	(Bendig et al., 2015)
EXB	Excess Blue Vegetation Index	$(1.4*B-G)/(G+R+B)$	(Maimaitijiang et al., 2019)
NDI	Normalized difference index	$(R-G)/(R+G)$	(Woebbecke et al., 1993)
EXR	Excess Red Vegetation Index	$1.4*R-B$	(Meyer and Neto, 2008)
EXGR	Excess Green minus Excess Red index	$ExG-ExR$	(Meyer and Neto, 2008)
RRATIO	Red Ratio	$R/(R+B+G)$	(Woebbecke et al., 1995)
BRATIO	Blue Ratio	$B/(R+B+G)$	(Woebbecke et al., 1995)
GRATIO	Green Ratio	$G/(R+B+G)$	(Woebbecke et al., 1995)
VARI	Visible Atmospherically Resistance Index	$(G-R)/(G+R-B)$	(Gitelson et al., 2002)
NRBI	Normalized Red Blue Index	$(R-B)/(R+B)$	(Michez et al., 2016)
NGBI	Normalized Green Blue Index	$(G-B)/(G+B)$	(Michez et al., 2016)
VEG	Vegetative index	$G/(RaB(1-a))$, where $a = 0.667$	(Hague et al., 2006)
WI	Woebbecke Index	$(G-B)/(R-G)$	(Woebbecke et al., 1995)
CIVE	Color Index of Vegetation	$0.441R - 0.881G + 0.385B + 18.78745$	(Kataoka et al., 2003)
COM	Combination Vegetative index	$0.25ExG + 0.3ExGR + 0.33CIVE + 0.12VEG$	(Guijarro et al., 2011)
TGI	Triangular Greenness Index	$G - 0.39R - 0.61B$	(Hunt et al., 2014; Michez et al., 2018)
RGBVI	Red Green Blue Vegetation Index	$(G2-B*R)/(G2+B*R)$	(Bendig et al., 2015)
GRR	Green Red Ratio Index	G/R	(Maimaitijiang et al., 2019)
GBRI	Green Blue Ratio Index	G/B	(Maimaitijiang et al., 2019)
RBRI	Red Blue Ratio Index	R/B	(Maimaitijiang et al., 2019)
BRRI	Blue Red Ratio Index	B/R	(Jibo et al., 2018)
BGRI	Blue Green Ratio Index	B/G	(Jibo et al., 2018)
RGRI	Red Green Ratio Index	R/G	(Jibo et al., 2018)
INT	Color Intensity Index	$(R+B+G)/3$	(Ahmad and Reid, 1996)
MVARI	Modified VARI	$(G-B)/(G+R-B)$	(Cen et al., 2019)
IPCA	Principal Component Analysis Index	$0.994 \times R-B + 0.961 \times G-B + 0.914 \times G-R $	(Saberioon et al., 2014)

616

617

618

Acronym	Index name	Formula	Reference
R	An average value of R channel of the quadrat-scale UAV imagephoto		
G	An average value of G channel of the quadrat-scale UAV imagephoto		
B	An average value of B channel of the quadrat-scale UAV photoimage		
H	An average value of H channel of the quadrat-scale image in HSV color space		
S	An average value of S channel of the quadrat-scale image in HSV color space		
V	An average value of V channel of the quadrat-scale image in HSV color space		
FVC	Fractional Vegetation Cover		
EGI	Extra Geen Index	$EGI = 2G - R - B$	
GI	Green Index	$GI = 9 \times (H \times 3.14159 / 180) + 3 \times S + V$	(Zhang et al., 2022a)
HOC_i_C ORR	The histogram correlation coefficient between the i band and the black reference histogram, where the i represents the three bands of RGB	$corr = \frac{\sum_l (H_1(I) - \bar{H}_1)(H_2(I) - \bar{H}_2)}{\sqrt{\sum_l (H_1(I) - \bar{H}_1)^2 \sum_l (H_2(I) - \bar{H}_2)^2}}$	
HOC_i INTERSE C	The histogram intersection coefficient between the i band and the black reference histogram, where the i represents the three bands of RGB	$intersec = \sum_l \min(H_1(I), H_2(I))$	
HOC_i BHATTA	The histogram Bhattacharyya distance coefficient between the i band and the black reference histogram, where the i represents the three bands of RGB	$\begin{aligned} & \text{bhatta} \\ & \equiv \sqrt{1 - \frac{1}{\sqrt{\bar{H}_1 \bar{H}_2 N^2}} \sum_l \sqrt{H_1(I) \cdot H_2(I)}} \\ & = \sum_l \min(H_1(I), H_2(I)) \end{aligned}$	
HOC_i_C HIS	The histogram correlation coefficient between the i band and the black reference histogram, where the i represents the three bands of RGB.	$chis = \sum_l \frac{(H_1(I) - H_2(I))^2}{H_1(I)}$	

621 **Table A4: Regression analysis for AGB estimation models at quadrat and pixel scales**

Model name	Coefficient	Value	Standard Error	t-Value	p-value
2019_Quadrat-scale	Slope	0.67	0.016	42.58	9.05e-194
	Intercept	20.10	1.49	13.59	5.96e-37
2019_Pixel_scale	Slope	0.84	0.03	31.59	2.75e-73
	Intercept	23.20	4.04	5.74	4.24e-8
2018_Pixel_scale	Slope	0.73	0.02	45.81	8.28e-157
	Intercept	20.43	2.74	7.46	6.01e-13
2017_Pixel_scale	Slope	0.75	0.01	59.13	1.98e-260
	Intercept	13.89	2.04	6.82	2.19e-11
2016_Pixel_scale	Slope	0.94	0.02	40.45	4.69e-157
	Intercept	2.48	3.75	0.66	0.03
2015_Pixel_scale	Slope	0.82	0.04	18.88	2.59e-47
	Intercept	9.50	5.25	1.81	0.04

622

623 **Table A5: List of abbreviations of eco-geographical regions and the mean AGB of the QTP**

Abbreviation	Full name
IB1	Golog-Nagqu high-cold shrub-meadow zone
HAB1	Western Sichuan-eastern Tibet montane coniferous forest zone
IC1	Southern Qinghai high-cold meadow steppe zone
IC2	Qiangtang high-cold steppe zone
ID1	Kunlun high-cold desert zone
IIAB1	Western Sichuan-eastern Tibet montane coniferous forest zone
IIC1	Southern Tibet montane shrub-steppe zone
IIC2	Eastern Qinghai-Qilian montane steppe zone
IID1	Nagri montane desert-steppe and desert zone
IID2	Qaidam montane desert zone
IID3	Northern slopes of Kunlun montane desert zone
OA1	Southern slopes of Himalaya montane evergreen broad-leaved forest zone

624

- 626 Ahmad, I. S. and Reid, J. F.: Evaluation of Colour Representations for Maize Images, *Journal of Agricultural Engineering Research*, 63,
627 185-195, doi:10.1006/jaer.1996.0020 1996.4
- 628 Bendig, J., Yu, K., Aasen, H., Bolten, A., Bennertz, S., Broscheit, J., Gnyp, M. L., and Bareth, G.: Combining UAV-based plant height
629 from crop surface models, visible, and near infrared vegetation indices for biomass monitoring in barley, *International Journal of Applied*
630 *Earth Observation & Geoinformation*, 39, 79-87, doi:10.1016/j.jag.2015.02.012, 2015.4
- 631 Bian, L. and Walsh, S. J.: Scale dependencies of vegetation and topography in a mountainous environment of Montana, *The Professional*
632 *Geographer*, 45, 1-11, doi:10.1111/j.0033-0124.1993.00001.x, 1993.4
- 633 Breiman, L.: Random forests, *Machine learning*, 45, 5-32, doi:10.1023/A:1010933404324, 2001.4
- 634 Camps-Valls, G., Campos-Taberner, M., Moreno-Martinez, A., Walther, S., Duveiller, G., Cescatti, A., Mahecha, M. D., Munoz-Mari, J.,
635 Garcia-Haro, F. J., Guanter, L., Jung, M., Gamon, J. A., Reichstein, M., and Running, S. W.: A unified vegetation index for quantifying
636 the terrestrial biosphere, *Sci Adv*, 7, eabc7447, doi:10.1126/sciadv.abc7447, 2021.4
- 637 Cannavacciuolo, M., Bellido, A., Cluzeau, D., Gascuel, C., and Trehen, P.: A geostatistical approach to the study of earthworm
638 distribution in grassland, *Applied Soil Ecology*, 9, 345-349, doi:10.1016/S0929-1393(98)00087-0, 1998.4
- 639 Cen, H. Y., Wan, L., Zhu, J. P., Li, Y. J., Li, X. R., Zhu, Y. M., Weng, H. Y., Wu, W. K., Yin, W. X., Xu, C., Bao, Y. D., Feng, L., Shou, J.
640 Y., and He, Y.: Dynamic monitoring of biomass of rice under different nitrogen treatments using a lightweight UAV with dual image-
641 frame snapshot cameras, *Plant Methods*, 15, doi:10.1186/s13007-019-0418-8, 2019.4
- 642 Chen, J., Yi, S., Qin, Y., and Wang, X.: Improving estimates of fractional vegetation cover based on UAV in alpine grassland on the
643 Qinghai-Tibetan Plateau, *International Journal of Remote Sensing*, 37, 1922-1936, doi:10.1080/01431161.2016.1165884, 2016.4
- 644 Cheng, X., An, S., Chen, J., Li, B., Liu, Y., and Liu, S.: Spatial relationships among species, above-ground biomass, N, and P in degraded
645 grasslands in Ordos Plateau, northwestern China, *Journal of Arid Environments*, 68, 652-667, doi:10.1016/j.jaridenv.2006.07.006, 2007.4
- 646 Crow, W. T., Berg, A. A., Cosh, M. H., Loew, A., Mohanty, B. P., Panciera, R., de Rosnay, P., Ryu, D., and Walker, J. P.: Upscaling
647 sparse ground - based soil moisture observations for the validation of coarse - resolution satellite soil moisture products, *Reviews of*
648 *Geophysics*, 50, doi:10.1029/2011rg000372, 2012.4
- 649 Dancy, K., Webster, R., and Abel, N.: Estimating and mapping grass cover and biomass from low-level photographic sampling,
650 *International Journal of Remote Sensing*, 7, 1679-1704, doi:10.1080/01431168608948961, 1986.4
- 651 Ding, M. J., Zhang, Y. L., Sun, X. M., Liu, L. S., Wang, Z. F., and Bai, W. Q.: Spatiotemporal variation in alpine grassland phenology in
652 the Qinghai-Tibetan Plateau from 1999 to 2009, *Chinese Science Bulletin*, 58, 396-405, doi:10.1007/s11434-012-5407-5, 2013.4
- 653 Dusseux, P., Hubert-Moy, L., Corpetti, T., and Vertes, F.: Evaluation of SPOT imagery for the estimation of grassland biomass,
654 *International Journal of Applied Earth Observation and Geoinformation*, 38, 72-77, doi:10.1016/j.jag.2014.12.003, 2015.4
- 655 Fensholt, R., Rasmussen, K., Nielsen, T. T., and Mbow, C.: Evaluation of earth observation based long term vegetation trends—
656 Intercomparing NDVI time series trend analysis consistency of Sahel from AVHRR GIMMS, Terra MODIS and SPOT VGT data, *Remote*
657 *sensing of environment*, 113, 1886-1898, 2009.4
- 658 Gao, X., Huete, A. R., Ni, W., and Miura, T.: Optical-biophysical relationships of vegetation spectra without background contamination,
659 *Remote sensing of environment*, 74, 609-620, 2000.4
- 660 Gao, X. X., Dong, S. K., Li, S., Xu, Y. D., Liu, S. L., Zhao, H. D., Yeomans, J., Li, Y., Shen, H., Wu, S. N., and Zhi, Y. L.: Using the
661 random forest model and validated MODIS with the field spectrometer measurement promote the accuracy of estimating aboveground
662 biomass and coverage of alpine grasslands on the Qinghai-Tibetan Plateau, *Ecological Indicators*, 112, 106114,
663 doi:10.1016/j.ecolind.2020.106114, 2020.4
- 664 Ghosh, S. M. and Behera, M. D.: Aboveground biomass estimation using multi-sensor data synergy and machine learning algorithms in a
665 dense tropical forest, *Applied Geography*, 96, 29-40, doi:10.1016/j.apgeog.2018.05.011, 2018.4
- 666 Gitelson, A. A., Kaufman, Y. J., Stark, R., and Rundquist, D.: Novel algorithms for remote estimation of vegetation fraction, *Remote*
667 *Sensing of Environment*, 80, 76-87, doi:10.1016/s0034-4257(01)00289-9 2002.4
- 668 Guijarro, M., Pajares, G., Riomoros, I., Herrera, P. J., Burgos-Artizzu, X. P., and Ribeiro, A.: Automatic segmentation of relevant textures
669 in agricultural images, *Computers & Electronics in Agriculture*, 75, 75-83, doi:10.1016/j.compag.2010.09.013, 2011.4
- 670 Hague, T., Tillett, N. D., and Wheeler, H.: Automated Crop and Weed Monitoring in Widely Spaced Cereals, *Precision Agriculture*, 7, 21-
671 32, doi:10.1007/s11119-005-6787-1, 2006.4
- 672 He, L., Li, A. N., Yin, G. F., Nan, X., and Bian, J. H.: Retrieval of Grassland Aboveground Biomass through Inversion of the PROSAIL
673 Model with MODIS Imagery, *Remote Sensing*, 11, 1597, doi:10.3390/rs11131597, 2019.4
- 674 Hoaglin, D. C., Mosteller, F., and Tukey, J. W.: Understanding robust and exploratory data analysis, *Wiley series in probability and*
675 *mathematical statistics*, 1983.4
- 676 Holben, B. N.: Characteristics of maximum-value composite images from temporal AVHRR data, *International journal of remote sensing*,
677 7, 1417-1434, 1986.4

678 Hunt, E. R., Daughtry, C. S. T., Mirsky, S. B., and Hively, W. D.: Remote Sensing With Simulated Unmanned Aircraft Imagery for
679 Precision Agriculture Applications, *IEEE Journal of Selected Topics in Applied Earth Observations & Remote Sensing*, 7, 4566-4571,
680 doi:doi:10.1109/jstars.2014.2317876, 2014.4

681 Jia, W., Liu, M., Yang, Y., He, H., Zhu, X., Yang, F., Yin, C., and Xiang, W.: Estimation and uncertainty analyses of grassland biomass in
682 Northern China: Comparison of multiple remote sensing data sources and modeling approaches, *Ecological indicators*, 60, 1031-1040,
683 doi:10.1016/j.ecolind.2015.09.001, 2016.4

684 Jiang, W., Yuan, L., Wang, W., Cao, R., Zhang, Y., and Shen, W.: Spatio-temporal analysis of vegetation variation in the Yellow River
685 Basin, *Ecological Indicators*, 51, 117-126, 2015.4

686 Jiao, C., Yu, G., He, N., Ma, A., and Hu, Z.: The spatial pattern of grassland aboveground biomass and its environmental controls in the
687 Eurasian steppe, doi:10.11821/dlxb201605007, 2017.4

688 Jibo, Y., Haikuan, F., Xiuliang, J., Huanhuan, Y., Zhenhai, L., Chengquan, Z., Guijun, Y., and Qingjiu, T.: A Comparison of Crop
689 Parameters Estimation Using Images from UAV-Mounted Snapshot Hyperspectral Sensor and High-Definition Digital Camera, *Remote
690 Sensing*, 10, 1138-, doi:10.3390/rs10071138, 2018.4

691 Kataoka, T., Kaneko, T., Okamoto, H., and Hata, S.: Crop growth estimation system using machine vision, *Advanced Intelligent
692 Mechatronics*, 2003. AIM 2003. Proceedings. 2003 IEEE/ASME International Conference on, Crop growth estimation system using
693 machine vision,

694 Kohavi, R.: A study of cross-validation and bootstrap for accuracy estimation and model selection, *Ijcai*, 1137-1145,
695 doi:10.1109/jstars.2014.2317876,

696 Li, M., Wu, J., Feng, Y., Niu, B., He, Y., and Zhang, X.: Climate variability rather than livestock grazing dominates changes in alpine
697 grassland productivity across Tibet, *Frontiers in Ecology and Evolution*, 9, doi:10.3389/fevo.2021.631024, 2021.4

698 Li, X., Liu, S., Li, H., Ma, Y., Wang, J., Zhang, Y., Xu, Z., Xu, T., Song, L., and Yang, X.: Intercomparison of six upscaling
699 evapotranspiration methods: From site to the satellite pixel, *Journal of Geophysical Research: Atmospheres*, 123, 6777-6803,
700 doi:10.1029/2018jd028422, 2018.4

701 Liu, S., Cheng, F., Dong, S., Zhao, H., Hou, X., and Wu, X.: Spatiotemporal dynamics of grassland aboveground biomass on the Qinghai-
702 Tibet Plateau based on validated MODIS NDVI, *Scientific reports*, 7, 1-10, doi:10.1038/s41598-017-04038-4, 2017.4

703 Louhaichi, M., Borman, M. M., and Johnson, D.: Spatially Located Platform and Aerial Photography for Documentation of Grazing
704 Impacts on Wheat, *Geocarto International*, doi:10.1080/10106040108542184,

705 Lussem, U., Bolten, A., Menne, J., Gnyp, M. L., Schellberg, J., and Bareth, G.: Estimating biomass in temperate grassland with high
706 resolution canopy surface models from UAV-based RGB images and vegetation indices, *Journal of Applied Remote Sensing*, 13, 034525,
707 doi:10.1117/1.Jrs.13.034525, 2019.4

708 Maimaitijiang, M., Sagan, V., Sidike, P., Maimaitiyiming, M., Hartling, S., Peterson, K. T., Maw, M. J. W., Shakoob, N., Mockler, T., and
709 Fritschi, F. B.: Vegetation Index Weighted Canopy Volume Model (CVM VI) for soybean biomass estimation from Unmanned Aerial
710 System-based RGB imagery, *ISPRS Journal of Photogrammetry and Remote Sensing*, 151, 27-41, doi:10.1016/j.isprsjprs.2019.03.003,
711 2019.4

712 Meng, B., Yi, S., Liang, T., Yin, J., and Sun, Y.: Modeling alpine grassland above ground biomass based on remote sensing data and
713 machine learning algorithm: A case study in the east of Tibetan Plateau, China, *IEEE Journal of Selected Topics in Applied Earth
714 Observations and Remote Sensing*, PP, 1-1, doi:10.1109/Jstars.2020.2999348, 2020.4

715 Meyer, G. E. and Neto, J. C.: Verification of color vegetation indices for automated crop imaging applications, *Computers and Electronics
716 in Agriculture*, 63, 282-293, doi:10.1016/j.compag.2008.03.009, 2008.4

717 Michez, A., Piégay, H., Lisein, J., Claessens, H., and Lejeune, P.: Classification of riparian forest species and health condition using multi-
718 temporal and hyperspatial imagery from unmanned aerial system, *Environmental Monitoring & Assessment*, 188, 1-19,
719 doi:10.1007/s10661-015-4996-2, 2016.4

720 Michez, A., Bauwens, S., Brostaux, Y., Hiel, M. P., Garré, S., Lejeune, P., and Dumont, B.: How Far Can Consumer-Grade UAV RGB
721 Imagery Describe Crop Production? A 3D and Multitemporal Modeling Approach Applied to Zea mays, *Remote Sensing*, 10,
722 doi:10.3390/rs10111798, 2018.4

723 Morais, T. G., Teixeira, R. F., Figueiredo, M., and Domingos, T.: The use of machine learning methods to estimate aboveground biomass
724 of grasslands: A review, *Ecological Indicators*, 130, 108081, doi:10.1016/j.ecolind.2021.108081, 2021.4

725 Mutanga, O. and Skidmore, A. K.: Narrow band vegetation indices overcome the saturation problem in biomass estimation, *International
726 journal of remote sensing*, 25, 3999-4014, 2004.4

727 Mutanga, O., Adam, E., and Cho, M. A.: High density biomass estimation for wetland vegetation using WorldView-2 imagery and random
728 forest regression algorithm, *International Journal of Applied Earth Observation and Geoinformation*, 18, 399-406,
729 doi:10.1016/j.jag.2012.03.012, 2012.4

730 Ômara, F. P.: The role of grasslands in food security and climate change, *Annals of botany*, 110, 1263-1270, doi:10.1093/aob/mcs209,
731 2012.4

732 Ramankutty, N., Evan, A. T., Monfreda, C., and Foley, J. A.: Farming the planet: 1. Geographic distribution of global agricultural lands in
733 the year 2000, *Global biogeochemical cycles*, 22, doi:10.1029/2007GB002952, 2008.4

734 Saberioon, M. M., Amin, M., Anuar, A. R., Gholizadeh, A., Wayayok, A., and Khairunniza-Bejo, S.: Assessment of rice leaf chlorophyll
735 content using visible bands at different growth stages at both the leaf and canopy scale, *International Journal of Applied Earth*
736 *Observations & Geoinformation*, 32, 35-45, doi:10.1016/j.jag.2014.03.018, 2014.4
737 Suttie, J. M., Reynolds, S. G., and Batello, C.: *Grasslands of the World*, Food & Agriculture Org.2005.
738 Tan, K., Ciaisi, P., Piao, S., Wu, X., Tang, Y., Vuichard, N., Liang, S., and Fang, J.: Application of the ORCHIDEE global vegetation model
739 to evaluate biomass and soil carbon stocks of Qinghai-Tibetan grasslands, 2010.4
740 Tucker, C. J.: Red and photographic infrared linear combinations for monitoring vegetation, *Remote Sensing and Environment*, 8, 127-150,
741 doi:10.1016/0034-4257(79)90013-0, 1979a.4
742 Tucker, C. J.: Red and photographic infrared linear combinations for monitoring vegetation, *Remote sensing of Environment*, 8, 127-150,
743 1979b.4
744 Vergara, J. R. and Estévez, P. A.: A review of feature selection methods based on mutual information, *Neural computing and applications*,
745 24, 175-186, doi:10.1007/s00521-013-1368-0, 2014.4
746 Viljanen, N., Honkavaara, E., Näsi, R., Hakala, T., Niemeläinen, O., and Kaivosoja, J.: A novel machine learning method for estimating
747 biomass of grass swards using a photogrammetric canopy height model, images and vegetation indices captured by a drone, *Agriculture*, 8,
748 70, doi:10.3390/agriculture8050070, 2018.4
749 Wang, J. and Sun, W.: Multiscale geostatistical analysis of sampled above-ground biomass and vegetation index products from HJ-1A/B,
750 Landsat, and MODIS, *Land Surface Remote Sensing II*, 2014.11, 335-344, doi:10.1117/12.2069008,
751 Wang, J., Ge, Y., Song, Y., and Li, X.: A geostatistical approach to upscale soil moisture with unequal precision observations, *IEEE*
752 *Geoscience and Remote Sensing Letters*, 11, 2125-2129, doi:10.1109/Lgrs.2014.2321429, 2014.4
753 Wang, J., Xiao, X., Bajgain, R., Starks, P., Steiner, J., Doughty, R. B., and Chang, Q.: Estimating leaf area index and aboveground
754 biomass of grazing pastures using Sentinel-1, Sentinel-2 and Landsat images, *ISPRS Journal of Photogrammetry and Remote Sensing*, 154,
755 189-201, doi:10.1016/j.isprsjprs.2019.06.007, 2019.4
756 Wang, L. a., Zhou, X., Zhu, X., Dong, Z., and Guo, W.: Estimation of biomass in wheat using random forest regression algorithm and
757 remote sensing data, *The Crop Journal*, 4, 212-219, doi:10.1016/j.cj.2016.01.008, 2016.4
758 Wang, Y., Shen, X., Jiang, M., Tong, S., and Lu, X.: Spatiotemporal change of aboveground biomass and its response to climate change in
759 marshes of the Tibetan Plateau, *International Journal of Applied Earth Observation and Geoinformation*, 102, 102385, 2021.4
760 Wang, Y., Wu, G., Deng, L., Tang, Z., Wang, K., Sun, W., and Shangguan, Z.: Prediction of aboveground grassland biomass on the Loess
761 Plateau, China, using a random forest algorithm, *Scientific reports*, 7, 1-10, doi:10.1038/s41598-017-07197-6, 2017.4
762 Woebbecke, D. M., Meyer, G. E., Bargaen, K. V., and Mortensen, D. A.: Color Indices for Weed Identification Under Various Soil,
763 Residue, and Lighting Conditions, *Transactions of the Asae*, 38, 259-269, doi:10.1109/jstars.2014.2317876 1995.4
764 Woebbecke, D. M., Meyer, G. E., Von Bargaen, K., and Mortensen, D. A.: Plant species identification, size, and enumeration using
765 machine vision techniques on near-binary images, *Optics in Agriculture and Forestry*, 208-219, 10.1117/12.144030
766 Xia, J., Ma, M., Liang, T., Wu, C., Yang, Y., Zhang, L., Zhang, Y., and Yuan, W.: Estimates of grassland biomass and turnover time on
767 the Tibetan Plateau, *Environmental Research Letters*, 13, 014020, doi:10.1088/1748-9326/aa9997, 2018.4
768 Yang, S., Feng, Q., Liang, T., Liu, B., Zhang, W., and Xie, H.: Modeling grassland above-ground biomass based on artificial neural
769 network and remote sensing in the Three-River Headwaters Region, *Remote Sensing of Environment*, S0034425717304741,
770 doi:10.1016/j.rse.2017.10.011, 2017.4
771 Yang, Y., Fang, J., Pan, Y., and Ji, C.: Aboveground biomass in Tibetan grasslands, *Journal of Arid Environments*, 73, 91-95,
772 doi:10.1016/j.jaridenv.2008.09.027, 2009.4
773 Yang, Y., Fang, J., Ma, W., Guo, D., and Mohammad, A.: Large - scale pattern of biomass partitioning across China's grasslands, *Global*
774 *Ecology and Biogeography*, 19, 268-277, doi:10.1111/j.1466-8238.2009.00502.x, 2010.4
775 Yi, S.: FragMAP: a tool for long-term and cooperative monitoring and analysis of small-scale habitat fragmentation using an unmanned
776 aerial vehicle, *International Journal of Remote Sensing*, 38, 2686-2697, doi:10.1080/01431161.2016.1253898, 2017.4
777 Yu, R., Yao, Y., Wang, Q., Wan, H., Xie, Z., Tang, W., Zhang, Z., Yang, J., Shang, K., and Guo, X.: Satellite-Derived Estimation of
778 Grassland Aboveground Biomass in the Three-River Headwaters Region of China during 1982–2018, *Remote Sensing*, 13, 2993,
779 doi:10.3390/rs13152993, 2021.4
780 Zeng, N., Ren, X., He, H., Zhang, L., Zhao, D., Ge, R., Li, P., and Niu, Z.: Estimating grassland aboveground biomass on the Tibetan
781 Plateau using a random forest algorithm, *Ecological Indicators*, 102, 479-487, doi:10.1016/j.ecolind.2019.02.023, 2019.4
782 Zhang, B., Zhang, L., Xie, D., Yin, X., Liu, C., and Liu, G.: Application of synthetic NDVI time series blended from Landsat and MODIS
783 data for grassland biomass estimation, *Remote Sensing*, 8, 10, doi:10.3390/rs8010010, 2016.4
784 Zhang, H., Sun, Y., Chang, L., Qin, Y., Chen, J., Qin, Y., Du, J., Yi, S., and Wang, Y.: Estimation of grassland canopy height and
785 aboveground biomass at the quadrat scale using unmanned aerial vehicle, *Remote sensing*, 10, 851, doi:10.3390/rs10060851, 2018.4
786 Zhang, H. F., Tang, Z. G., Wang, B. Y., Meng, B. P., Qin, Y., Sun, Y., Lv, Y. Y., Zhang, J. G., and Yi, S. H.: A non-destructive method
787 for rapid acquisition of grassland aboveground biomass for satellite ground verification using UAV RGB images, *Global Ecology and*
788 *Conservation*, 33, e01999, doi:10.1016/j.gecco.2022.e01999, 2022a.4

789 Zhang, X., LI, M., WU, J., HE, Y., and NIU, B.: Alpine Grassland Aboveground Biomass and Theoretical Livestock Carrying Capacity on
790 the Tibetan Plateau, *Journal of Resources and Ecology*, 13, 129-141, 2022b.4
791 Zhang, Y., Bingyu, L. I., and Zheng, D.: Datasets of the boundary and area of the Tibetan Plateau, *ACTA GEOGRAPHICA SINICA*, 69,
792 164-168, 2014.4
793 Zhang, Y. Q., Tang, Y. H., and Jiang, J. A.: Characterizing the dynamics of soil organic carbon in grasslands on the Qinghai-Tibetan
794 Plateau, 2007.4
795 Zheng, D.: Natural region system research of Tibetan Plateau, *Science in China (Series D)*, 26, 336–334, 1996.4